Ph.D. DISSERTATION

Efficient Integration of Barometric Pressure Sensors and Si FET-type Gas Sensors on the Same Substrate

실리콘 기판 위에 효율적으로 집적한 기압 센서와 FET형 가스 센서

By

Dongkyu Jang

August 2020

DEPARTMENT OF ELECTRICAL ENGINEERING AND COMPUTER SCIENCE

COLLEGE OF ENGINEERING

SEOUL NATIONAL UNIVERSITY

ABSTRACT

Sensor technology is becoming increasingly important to improve the quality of human life. Especially, various kinds of sensor technology have become essential due to increasing demand for smart mobile devices, automobiles and household appliances. Furthermore, as many types of sensors are installed on smart devices, it is more important to integrate different sensors in the IoT era. If multiple types of sensors are efficiently integrated with CMOS circuit on a single substrate, the footprint and power consumption could be reduced. Gas sensors are not only for detecting harmful gases, but also for improving indoor air quality and detecting diseases. The conventional resistor-type gas sensors have a simple structure and a simple manufacturing process, but they are large in size and have high power consumption. On the other hand, FET-type gas sensors can be fabricated very small in size and compatibly integrated with CMOS circuits, and they are easy to integrate with other types of sensors. In addition, built-in localized micro-heater can minimize power consumption of the FET-type gas sensors.

In this dissertation, barometric pressure sensors and Si FET-type gas sensors are efficiently integrated on the same Si substrate using conventional MOSFET fabrication process. The barometric pressure sensors have built-in temperature

sensors to accurately measure the atmospheric pressure according to the ambient temperature. In addition, the FET-type gas sensor has a localized micro-heater capable of heating up to 124 ºC with a power of 4 mW. NO_2 gas sensing is successfully achieved with this gas sensor.

Air-gap with a depth of 2.5 μm are formed in the Si substrate and used as the cavity for the barometric pressure sensor and as an insulating layer for the FET-type gas sensor. In addition, poly-Si with Boron ion implantation is used as the piezo-resistors of the barometric pressure sensor, the electrode of the temperature sensor, and the FG and micro-heater of the FET-type gas sensor at the same time. In this way, the barometric pressure sensors and the FET-type gas sensors are efficiently integrated using CMOS compatible fabrication process.

The barometric pressure sensor has a built-in temperature sensor that can measure ambient temperature and atmospheric pressure at the same time. The measured atmospheric pressure varies with ambient temperature, but with a designed neural network, accurate atmospheric pressure can be obtained with an accuracy of 97.5 %.

Keywords: Integration of sensors, Gas sensors, Barometric pressure sensors, Air-gap.

Student Number: 2016-30211

CONTENTS

List of figures

List of tables

Chapter 1. Introduction

1.1. Sensor technology

1.1.1. Various types of sensors

Various sensor technologies are applied in many industrial fields and they give great contributions to human life [1-13]. Sensor technologies are essential for climate prediction, medical diagnosis, altitude measurement, industrial safety, and air quality measurement [14-16]. Many types of sensors are installed in automobiles, medical devices, home appliances and smart devices. Especially, in the Internet of Things (IoT) era, research and development of highly sensitive and miniaturized sensors are constantly studied [17-26]. Accordingly, gyro sensors, gas sensors, pressure sensors, temperature sensors, and many other types of sensors are being studied [1-19], and new sensor technologies are being studied.

The demands of these sensor technologies are expected to increase, and the development of more sensitive, smaller and low power sensors are required.

1.1.2. Conventional MEMS sensors

Most sensors are fabricated using Micro Electro Mechanical System (MEMS) process technology. MEMS process technology has been widely applied in sensor fabrication. Economies of scale, the availability of high-quality materials and the ability to integrate electrical functions have expanded the field of Silicon MEMS sensor applications. MEMS sensors fabricated on Silicon (Si) substrates can be manufactured using semiconductor process technology, so they are inexpensive, highly compatible, and are easy for mass production [1-5, 13-17]. Most MEMS sensors are made by a general semiconductor process that makes the required shape through deposition, patterning through photolithography, and etching, and then normally post-processed [5-10, 13-17]. However, sensors fabricated by

MEMS process technology are large in size and not compatible with conventional Complementary Metal Oxide Semiconductor (CMOS) process technology [18-20]. As MEMS process technology use many kinds of nano-materials and solutions that are not compatible with conventional CMOS process, so particle contamination or ion diffusion problems can easily occur [21-22]. Therefore, it is almost impossible to fabricate the CMOS circuits and MEMS sensors on the same Si substrate. In order to make sensors compatible with CMOS process technology, process design of sensors must be done with new structures and layout based on the conventional CMOS process technology. In addition, after finishing the backend of line process with CMOS process technology, post processed should be performed to prevent the contamination from nano-materials or sensing materials. When sensors are fabricated by CMOS process technology, various sensors and CMOS circuit can be easily integrated on Si substrate [24, 25]. As far as we know, no technology reported to effectively integrates several sensors and Metal Oxide Semiconductor Field Effect Transistor (MOSFET)s on the Si substrate using

CMOS process technology and verify the operation of sensors and MOSFETs [24, 25].

1.2. Barometric Pressure Sensors

1.2.1. MEMS barometric pressure sensors

The barometric pressure sensors are used in many areas such as weather forecasting, altitude measurement and industrial measurement and the installation of barometric pressure sensors in automobiles and mobile devices is increasing [1-18]. The structure of the barometric pressure sensors and the pressure sensors are almost the same, and the principle of operation is also almost the same [1-16]. As MEMS based barometric pressure sensors have small size and good characteristics, they had replaced the conventional aneroid barometer. Most of MEMS barometric pressure sensors are fabricated by building a cavity under the Si substrate and sealing it [4-8]. The cavity can be built by back-side etching process of Si substrate or Potassium Hydroxide (KOH) wet solution etching process through the etching holes [1-12]. However, these methods require quite large area and process control is difficult as well. In addition, they are

incompatible with CMOS technology. The barometric pressure sensors fabricated by these MEMS processes have a pretty thick diaphragm, so the sensitivities of the sensors are relatively low [2-15]. Therefore, to improve the sensitivity of the MEMS barometric pressure sensors, large area diaphragms are required.

1.2.2. Diaphragm of barometric pressure sensors

Since Si diaphragm is easy to fabricate in the process, most MEMS barometric pressure sensors use Si diaphragm [1-13]. In addition, when ion impurities are implanted into Si, it can be easily obtained the piezo-resistance. Typical MEMS barometric sensors build a diaphragm with a thickness of 50 μm ~ 200 μm through the back-side etching process of Si substrate [5-13]. Since the back-side etching process of Si substrate is difficult to detect the end-point of etching process, fabricated diaphragm is quite thick and its uniformity is bad. In addition, Si has a relatively larger Young's modulus (130 GPa) than Young's

modulus of Silicon Dioxide (SiO_2) (66 GPa), so Si diaphragm shows a relatively smaller strain than SiO_2 diaphragm at the same pressure (Table 1.1). To overcome these shortcomings, the area of MEMS barometric pressure sensors which has a Si diaphragm is typically over 1 mm^2.

Table 1.1 Comparison of mechanical properties of materials used in CMOS process technology.

	Young's modulus (GPa)	**Poisson's ratio**
Si	**130**	**0.22**
SiO_2	**66**	**0.17**
Si_3N_4	**169**	**0.27**

1.2.3. Cavity in barometric pressure sensors

MEMS barometric pressure sensors measure the pressure difference between the cavity and the ambient air pressure [5-9]. The cavity of sensors is typically sealed under low vacuum or atmospheric pressure [17-19]. Normally, Si substrate

of sensor is etched on the back-side and then sealed by glass bonding (Fig. 1.1 (a)) [1]. There is also the method of closing the etching hole after etching Si substrate using KOH solution (Fig. 1.1 (b)) [2]. Another method is to form a cavity with an isotropic etching process through many small-sized etching holes in Si, and then seal the Si etching holes through epitaxial growth of Si (Fig. 1.1 (c)) [3]. However, this method is rarely used because it is expensive and formed cavity is shallow and the diaphragm is quite thick.

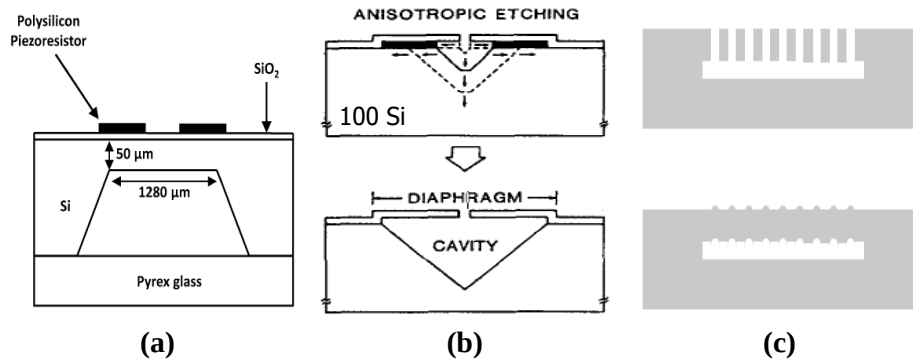

Fig. 1.1 Various ways to form the cavity of the barometric pressure sensors. (a) Si substrate of sensor is etched on the back-side and then sealed by glass bonding [1], (b) closing the etching hole after etching Si substrate using KOH solution [2], (c) form a cavity with an isotropic etching process through many small-sized etching holes in Si, and then seal the Si etching holes through epitaxial growth of Si [3].

1.2.4. Types of barometric pressure sensors

When the pressure between the ambient air pressure and the cavity changes, the pressure applied to the diaphragm changes and the diaphragm deforms

sequentially. There are two ways to read the deformation of diaphragm as an electrical signal. The one is capacitive-type (Fig. 1.2 (a)) [4] and the other is piezo-resistive-type (Fig. 1.2 (b)) [3]. Table 1.2 shows the characteristics of each barometric pressure sensor. The capacitive-type is a method of reading the change in capacitance between electrodes due to changes in barometric pressure by placing each electrode on the bottom of the cavity and under the diaphragm [4, 16, 20]. The capacitive-type has the disadvantage of requiring a very large area, but has better reliability than the piezo-resistive-type. The piezo-resistive-type reads the change of piezo-resistance of the piezo-resistor located on the diaphragm [1, 3, 7-11, 17-19, 21, 23, 31, 32]. The piezo-resistor can be made by implanting high concentration of ions into Si or Polycrystalline Silicon (poly-Si). The piezo-resistance change according to the ambient air pressure of the piezo-resistive-type pressure sensor is amplified and read by the Wheatstone bridge circuit composed of the piezo-resistors [1, 3, 7-11]. Since the piezo-resistive-type has a small size and high sensitivity, the currently widely used MEMS barometric pressure sensor

is the piezo-resistive-type.

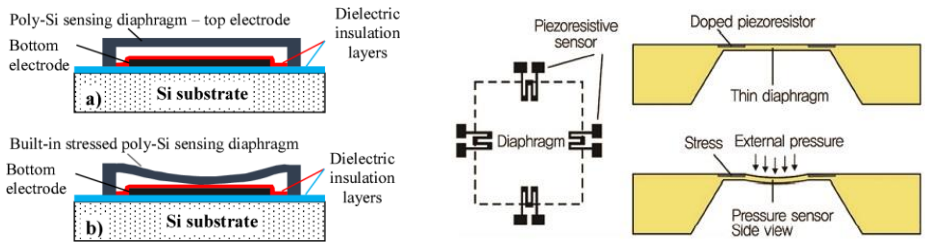

(a) **(b)**

Fig. 1.2 (a) Capacitive-type barometric pressure sensor [4], (b) piezo-resistive-type barometric pressure sensor [3].

Table 1.2 Comparison of characteristics between capacitive-type barometric pressure sensor and piezo-resistive-type barometric pressure sensor.

	Capacitive-type	**Piezo-resistive-type**
Working principle	**Capacitance change between electrodes**	**Piezo-resistive effect of electrodes**
Advantages	**More reliable**	**Small in size, High sensitivity**
Disadvantages	**Large in size**	**Less reliable**

1.3. Gas Sensors

1.3.1. Resistor-type gas sensors

Gas sensors are widely used in air quality measurement, medical diagnosis and industrial safety. In addition, the mounting of gas sensors in household appliances and mobile devices is increasing. Therefore, research and study on gas sensors has been actively conducted, and several types of gas sensors have attracted attention. The most commonly used and studied type is the resistor-type gas sensors [6, 33-54]. The resistor-type gas sensors read the change in the resistance of the sensor when exposed to the target gases. In order to obtain a proper operating temperature to detect the target gas, the resistor-type gas sensors usually have a built-in heater [26, 43-44]. The resistor-type gas sensors have the advantages of simple structure (Fig. 1.3) [5] and easy to fabricate. Most resistor-type gas sensors are simply fabricated using MEMS process technology [33-54]. Thanks to these advantages, it is easy to apply various sensing materials, such as

carbon nano-materials [37-39], semiconducting metal oxides [5, 20] and transition metal dichalcogenides [33-36], to the resistor-type gas sensors. Besides, in order to improve the sensitivity of the resistor-type gas sensors, researches on the morphology and chemical functionalization of the sensing materials are being studied [36, 37]. However, these resistor-type gas sensors require a large area and a large amount of current to obtain the sensing material at the operating temperature, resulting in high power consumption.

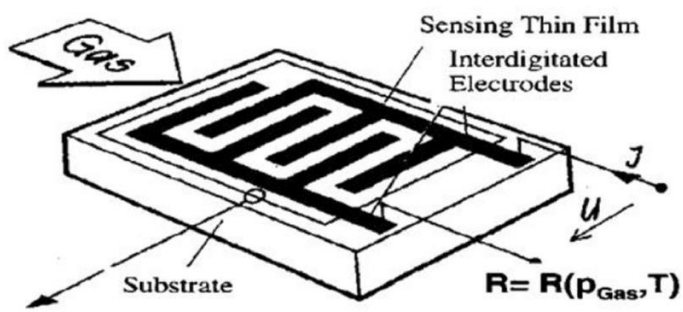

Fig. 1.3 Schematic structure of resistor-type gas sensor [5].

1.3.2. FET-type gas sensors

In order to solve the disadvantages of the resistor-type gas sensors, Field

Effect Transistor (FET) -type gas sensors are being studied [29, 55, 56]. The FET-type gas sensors use a sensing material as a gate or channel of the FET, and when exposed to a target gas, a change in the threshold voltage (V_{th}) or drain current (I_D) of the FET occurs. Since the FET-type gas sensors are compatible with the conventional CMOS process, it is possible to fabricate an CMOS circuit for adjusting the output signals or calibrating the differences due to the environmental changes such as humidity or ambient temperature. In addition, the FET-type gas sensors have high sensitivity and high accuracy even in small-sized sensing materials, and power consumption can be reduced by installing a small-sized localized micro-heater. Furthermore, since they can be fabricated using conventional CMOS process, they can be mass-manufactured as a single chip with an integrated circuit at a low cost [24. 25].

There are mainly two types of FET-type gas sensors. One is Thin Film Transistor (TFT) gas sensors [6, 52, 53], and the other is Si FET having a horizontal floating-gate (FG) [25, 26, 29]. TFT gas sensors use a sensing material

as its channel or active layer to detect target gases. Fig. 1.4 shows schematic cross-sectional view of the TFT gas sensor [6]. TFT gas sensors have three terminals (gate, source and drain), and these sensors read the change of the charge transfer or redistribution in its active layer when it exposed to target gases. However, theses TFT gas sensors are smaller in size than resistor-type gas sensors, but still require a large sensing area for stable output. In addition, since they are normally fabricated using MEMS process technology, it is difficult to integrate with CMOS circuits, and performance can be degraded due to the contamination by the sensing materials.

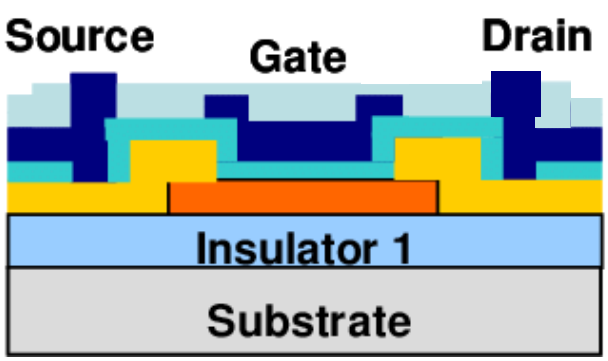

Fig. 1.4 Schematic cross-sectional view of TFT gas sensor [6].

To solve the shortcomings of TFT gas sensors, our group proposed a Si FET-type gas sensor having a horizontal FG [26, 29]. Fig. 1.5 (a) is a top view SEM image showing the structure of the gas sensors with a horizontal FG based on MOSFET that we already proposed [29]. And Fig. 1.5 (b) shows the schematic cross-sectional view of the sensors. Because this MOSFET-based gas sensor uses conventional CMOS process technology, so it can be fabricated at low cost, small in size and integrated with CMOS circuits. In addition, this gas sensor can be used as a platform for various gas sensing, as different types of sensing materials are available. The MOSFET used in the gas sensor is protected with a layer of Silicon Nitride (Si_3N_4), and the sensing material is deposited at the final step of device fabrication, so the MOFET is completely protected from contamination of the sensing material. Moreover, as some fingers of the FG engage the control-gate (CG) in the horizontal direction, the gas sensor exhibits excellent performance with a high coupling ratio.

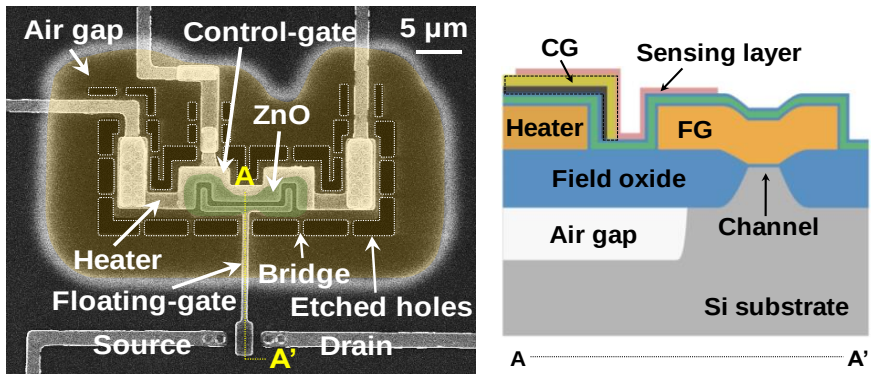

Fig. 1.5 (a) top view SEM image showing the structure of the gas sensors with a horizontal FG, (b) schematic cross-sectional view of the sensors [26].

1.3.3. Heater and air-gap in gas sensors

Gas detection for various types of target gases is being studied: Nitrogen Dioxide (NO_2) [41, 48], Hydrogen Sulfide (H_2S) [56], Ammonia (NH_3), Carbon Dioxide (CO_2) [39], Methane (CH_4), and so on. Various types of sensing materials are used to detect these gases: semiconducting metal oxides, carbon nano-materials and transition metal dichalcogenides. Among them, the most widely studied sensing materials are semiconducting metal oxides: Zinc Oxide (ZnO)

[26], Tin Dioxide (SnO_2) [36, 43], Indium Oxide (In_2O_3) [25, 34] and so on. Each metal oxide has an optimal operating temperature that responds well to the specific target gas. For example, the gas sensor using a ZnO film as a sensing material shows an optimal operating temperature of 180 ºC in NO_2 gas and a suitable operating temperature of 150 ºC in H_2S gas. In general, gas sensors using metal oxide as a sensing material show efficient gas detection characteristics in the range of 150-400 ºC.

In order to make the gas sensors at the proper operating temperature, a heater and air-gap must be installed [25, 26]. A heater is required to raise the suitable operating temperature for gas detection from room temperature, and the air-gap is essential to prevent heat loss and maintain temperature. In general, Platinum (Pt) and Tungsten (W) are widely used as the heater for gas sensors [43, 44], and our group reported heavily doped poly-Si as the heater [25, 26]. Table 1.2 shows the thermal conductivities of typical materials used in CMOS process technology. Since the thermal conductivity of Si (130 W/m·K) used as the substrate of the gas

sensors is very large, the gas sensor cannot maintain the proper operating temperature without preventing heat dissipation through the Si substrate. As shown in Table 1.3, the thermal conductivity of air is extremely low, most gas sensors form an air-gap etched on the backside of Si substrate to prevent heat dissipation [43, 44]. However, the heaters used in the gas sensors are large in size, so they have high power consumption. In addition, the process of forming air-gap is complicated and is not compatible with CMOS process technology. Therefore, it is necessary to develop an efficient and low-power gas sensor by localizing the micro-heater only around the sensing materials and forming an air-gap only on the sensing materials [26]. In addition, the process for forming the air-gap compatible with CMOS process technology is required.

Table 1.3 Thermal conductivities of typical materials used in CMOS process technology.

	Thermal conductivity (W/m·K)
Air	**0.024**
Si	**130**
Poly-Si	**30-40**
SiO_2	**1.4**
Si_3N_4	**9-30**
Cr	**93.7**
Au	**317**
Al	**205**
Cu	**385**
W	**173**

1.4. Integration of various types of sensors

Various sensors have been developed to help human life. Many types of sensors are still being studied and the demand for these sensors will increase [1-13, 25-31]. In order to efficiently control and function various sensors, it is important to integrate the sensors on one chip [24]. Integrating different type of sensors on one chip can reduce fabrication cost and lower power consumption of the sensors. In addition, by integrating CMOS circuits with various sensors, power consumption can be extremely lowered and the functions of the sensors can be enhanced. In particular, it is possible to build a smart sensor system by applying Artificial Intelligence (AI) composed of CMOS circuits, which has recently attracted attention. Therefore, it is important to develop the CMOS compatible process that is commonly applicable to various types of sensors.

1.5. Purpose of research

In this dissertation, study is carried out with the goal of the integration of different sensors. As far as we know, no technology has been reported to efficiently integrate different types of sensors onto a single chip. We propose the fabrication technology that efficiently integrated the barometric pressure sensors and the FET-type gas sensors. The key factors are the process of forming air-gap that can be used in common for both sensors, and poly-Si, which is used in various ways. In addition, the fabrication and verification of MOSFET with the sensors and integrating CMOS circuits with the sensors are also discussed.

1.6. Dissertation outline

This dissertation is organized as follows. Chapter 1 contains an overview of sensor technology by introducing various types of sensors. In particular, conventional barometric pressure sensor technologies and various types of gas sensors are reviewed. Then the importance of integrating various types of sensors is described. The purpose of study and the dissertation outline are also presented. In Chapter 2, the structure and the layout of the fabricated sensors are explained in detail. In addition, the main fabrication process of the sensors and the key factors necessary for integrating different sensors are presented. Chapter 3 describes the characteristics of the fabricated sensors. Especially, the simulation results of the sensors proposed in this study and the measurement results of the fabricated sensors are presented in detail. In addition, the operating principles of the fabricated sensors are also described. Finally, the conclusion is presented in Chapter 4.

Chapter 2. Device structure and fabrication

2.1. Integration of different sensors

In this dissertation, FET-type gas sensor having a horizontal FG and micro-heater and barometric pressure sensors having a built-in temperature sensor are fabricated simultaneously on the same Si substrate [24, 25]. Two different types of sensors are integrated on a single Si wafer, and they are efficiently fabricated in an optimal process. Fig. 2.1 shows an optical top view of the integrated barometric pressure sensors and FET-type gas sensor on the Si substrate. As shown in Fig. 2.1, barometric pressure sensors and FET-type gas sensor are located adjacently. Barometric pressure sensors and FET-type gas sensor have their own probing pad and can be operated individually.

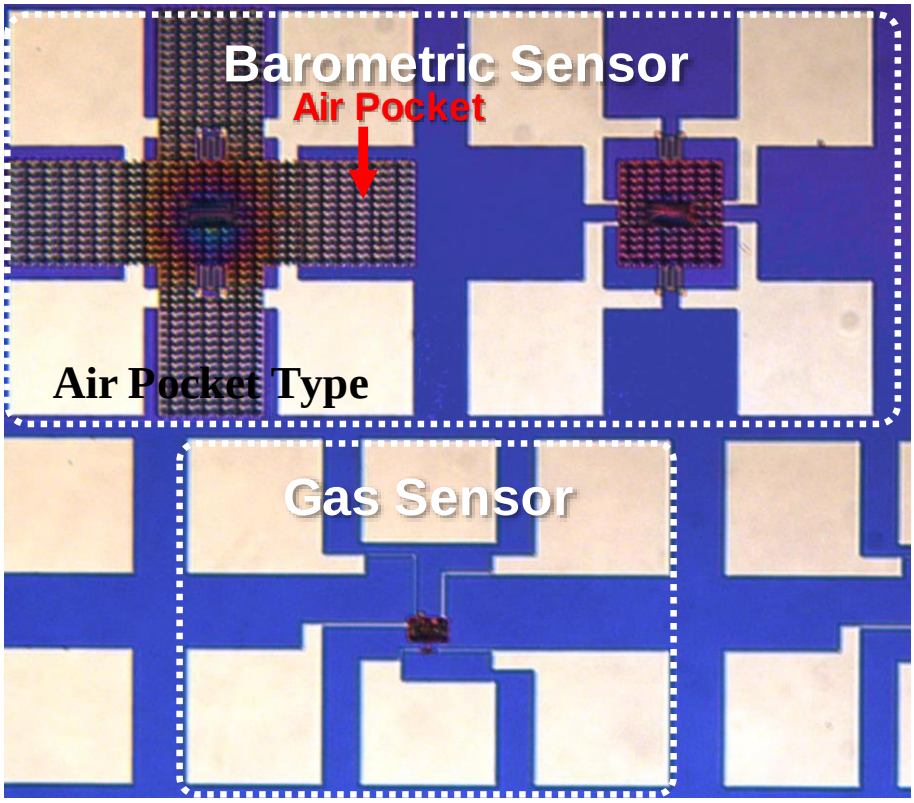

Fig. 2.1 Optical plan view of the barometric sensor and the gas sensor fabricated on the same substrate.

2.2. Structure of barometric pressure sensors

2.2.1. Air pocket of barometric pressure sensors

Barometric pressure sensors are fabricated in two type: an air pocket type (Fig. 2.2 (a)) and a normal type (Fig. 2.2 (b)) [24, 25]. The air pocket type barometric pressure sensor increased the sensitivity of the sensor by adding air pockets around the sensor and air pockets are all connected to the sensor through the cavity. Air pockets are formed when the cavity of the barometric pressure sensor is formed, and anchors are arranged in all areas of air pockets. These air pockets increase the stress on the central diaphragm of the barometric pressure sensor. Fig. 2.3 (a) is a cross-sectional Scanning Electron Microscopy (SEM) view of the central region of the diaphragm, and Fig. 2.3 (b) is a cross-sectional SEM view of the air pocket and the area excluding the central region of the diaphragm. As shown in Fig. 2.3 (b), Si column support the diaphragm and we named this as anchor. Anchors of 3 × 3 μm are placed except for central region of the barometric

pressure sensor, the diaphragm except the central region does not move according to the pressure difference. This ensures that stresses due to pressure differences are concentrated only in the central region.

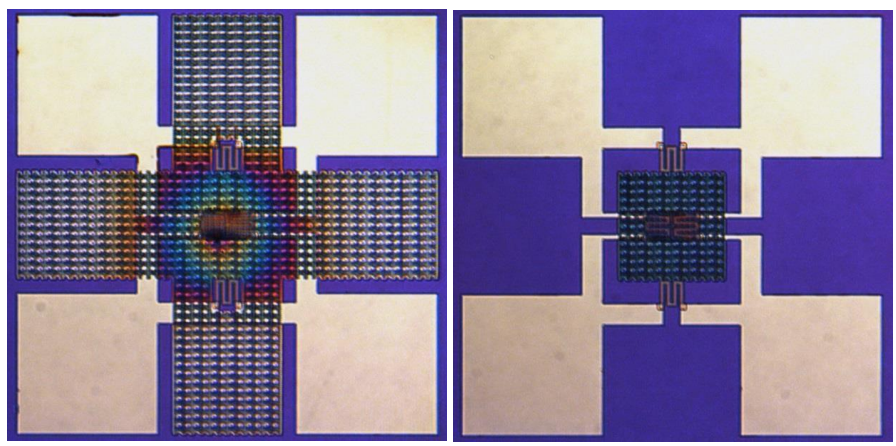

(a) **(b)**

Fig. 2.2 (a) Air pocket type and (b) normal type barometric pressure sensors.

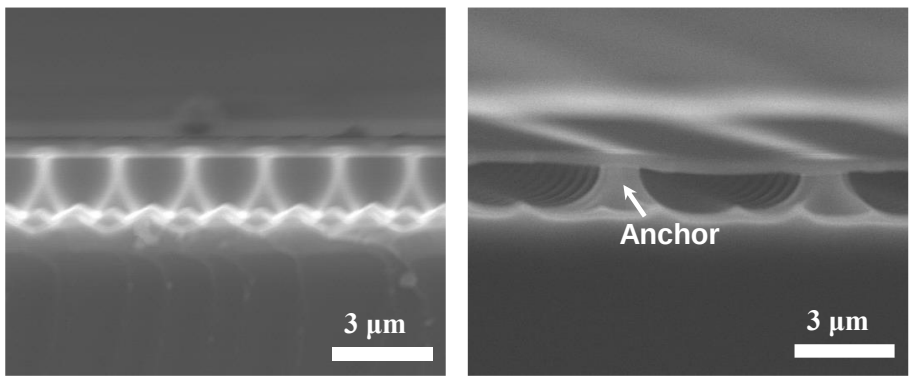

Fig. 2.3 (a) Cross-sectional SEM view of the central region and (b) air pocket and the area excluding the central region of the diaphragm.

2.2.2. New design of piezo-resistor

Fig. 2.4 (a) is a top view SEM image of a conventional piezo-resistor widely used in barometric pressure sensors. As shown in Fig. 2.4 (a), piezo-resistors using heavy Boron (B) doped poly-Si are placed on the barometric pressure sensor. Two piezo-resistors are placed on the movable diaphragm in the central region of the barometric pressure sensor, and two piezo-resistors are placed in the area without the cavity. Piezo-resistors placed on the diaphragm that can move according to the

changes in atmospheric pressure become variable resistors, and piezo-resistors located on the Si substrate which doesn't have a cavity become fixed resistors. These four piezo-resistors are composed of a Wheatstone bridge circuit with two variable resistors and two fixed resistors (Fig. 2.4 (c)) [13]. The Wheatstone bridge circuit amplifies the change of piezo-resistance due to the change in atmospheric pressure to output voltage (V_{out}) is

$$V_{out} = \frac{(R_1 \times R_3) - (R_2 \times R_4)}{(R_1 + R_2) \times (R_3 + R_4)} \times V_{in} \quad (1)$$

To reduce the noise and increase the sensitivity of the Wheatstone bridge circuit, the resistance values (R) of the four piezo-resistors should be the same as possible. When the resistance change (ΔR) of two variable resistors is the same, V_{out} is as follows [23].

$$V_{out} = \frac{\Delta R}{(2R + \Delta R)} \times V_{in} \quad (2)$$

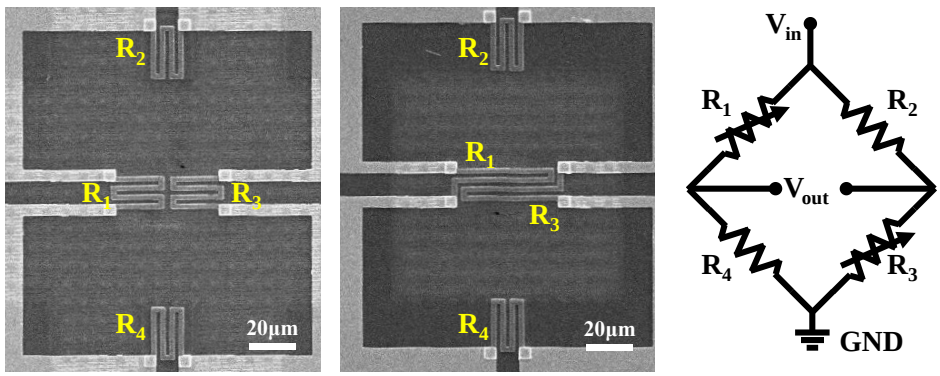

(a) **(b)** **(c)**

Fig. 2.4 (a) Magnified top view SEM image of barometric pressure sensors with conventional piezo-resistors and (b) new design piezo-resistors, (c) Equivalent circuit of Wheatstone bridge composed of two variable resistors and two fixed resistors.

In this dissertation, we propose a new design of piezo-resistors with a higher sensitivity than the conventional piezo-resistor used in previous barometric pressure sensors. As shown in the Fig. 2.4 (b), the proposed piezo-resistors used as variable resistors are designed longer than the conventional piezo-resistors. The proposed variable piezo-resistors have the same *R* as fixed piezo-resistors with the

same design as conventional piezo-resistors, and are placed on the end point from the beginning of the bendable central region of the diaphragm. The variable piezo-resistors placed on the conventional barometric pressure sensors have relatively little ΔR because they are located only half of the movable diaphragm. However, since the proposed piezo-resistors are located in the entire central region of the movable diaphragm, the piezo-resistance change are designed to be expected to be much larger. The behaviors of the proposed new design of piezo-resistors are verified by COMSOL Multiphysics simulations and measurements of the fabricated barometric pressure sensors [28].

2.3. Structure of FET-type gas sensors

2.3.1. Structure and layout of FET-type gas sensors

Fig. 2.5 (a) is a top view SEM image of the FET-type gas sensor having FG and micro-heater fabricated in this study [25]. Fig. 2.5 (b) is a cross-sectional schematic view of the FET-type gas sensor. Since *p*MOSFET has less flicker noise than *n*MOSFET, FET-type gas sensors in this dissertation are fabricated as *p*MOSFET. In addition, to further reduce the noise of the *p*MOSFET, *p*MOSFETs with a buried channel are fabricated [26, 29]. As shown in Fig., FG and CG are formed horizontally in the form of meshing with each other, thereby increasing the coupling ratio between them. A gap between the FG and the CG is 0.5 μm, and an *n*-type semiconducting Indium oxide (In_2O_3) layer is used as a sensing material to fill the space between the FG and CG. Poly-Si with heavy B ion implantation is used as the FG and the micro-heater.

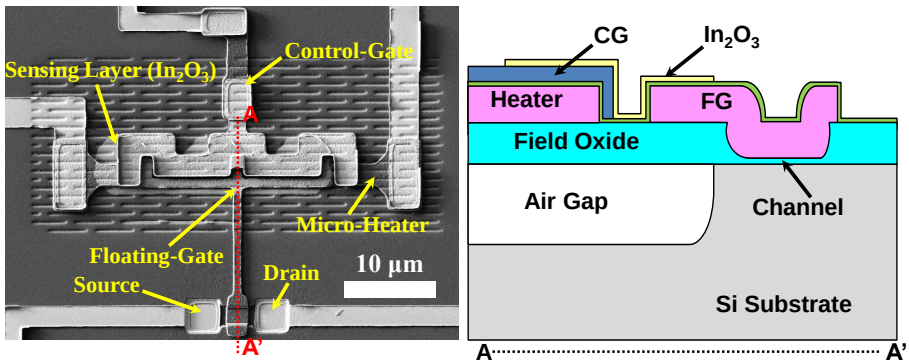

Fig. 2.5 (a) Top view SEM image and (b) cross-sectional schematic view of FET-type gas sensor having FG and micro-heater.

The micro-heater is localized so that only the temperature of the gas sensing part can be raised, and the air-gap with a depth of 2.5 μm is formed below the gas sensor to prevent heat dissipation of the gas sensing part. In addition, the air-gap also prevents heat generated by the micro-heater from diffusing to the channel of the MOSFET, thereby guaranteeing stable operating of the MOSFET [26, 43, 44]. The MOSFET of the FET-type gas sensor has a channel width of 2 μm and a channel length of 2 μm. The FG and the micro-heater are covered with SiO_2 (10

nm) /Si_3N_4 (20nm) /SiO_2 (10 nm) (ONO) layers, which is electrically insulated from the CG and the gas sensing part. The gas sensing part is electrically insulated from the FG by the ONO layers, but is connected to the CG, so it operates as a gate of the MOSFET. The Si_3N_4 film of ONO layers also prevent the MOSFET from being contaminated from the gas sensing part.

2.4. Device fabrication

2.4.1. Key fabrication process

Barometric pressure sensors and FET-type gas sensors having a horizontal floating-gate and micro-heater are fabricated on a Si substrate using conventional CMOS process technology [25]. Total six photo masks are used in the entire fabrication. 6-inch p-type (100) bulk Si wafer is used to fabricate barometric pressure sensors and FET-type gas sensors. Fig. 2.6 shows the main steps of fabrication process. After RCA chemical cleanings which include SPM (H_2SO_4, H_2O_2), SC1 (H_2O_2, NH_4OH, DI H_2O), SC2 (H_2O_2, HCl, DI H_2O) and HF are performed on the bulk Si wafer, the ion implantation process is carried out to build *N*-well of the *p*MOSFET. Then thermal SiO_2 layer having a thickness of 300 nm is grown. The SiO_2 layer is patterned with line-shaped etching holes of 0.5 μm diameter using the first photo mask (Fig. 2.7 (a), Fig. 2.10 (a)). 3 × 3 μm^2 non-etched square SiO_2 patterns are left with 8 μm spacing between line-shaped

etching holes to form Si anchors.

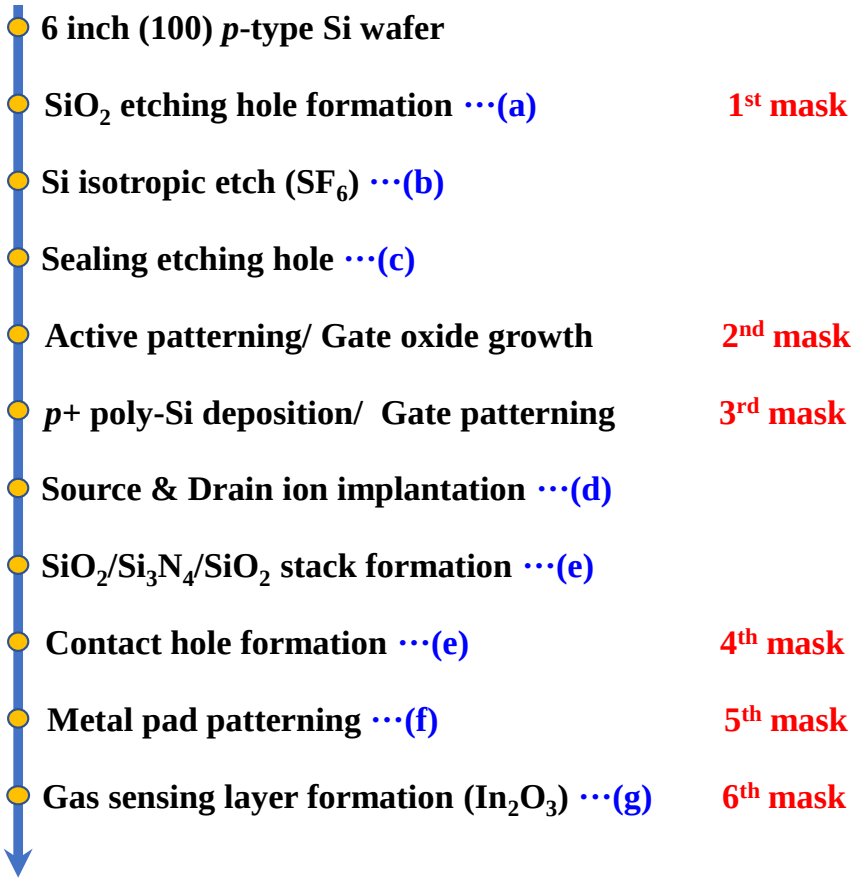

Fig. 2.6 Main steps of fabrication process of integrated barometric pressure sensors and FET-type gas sensors.

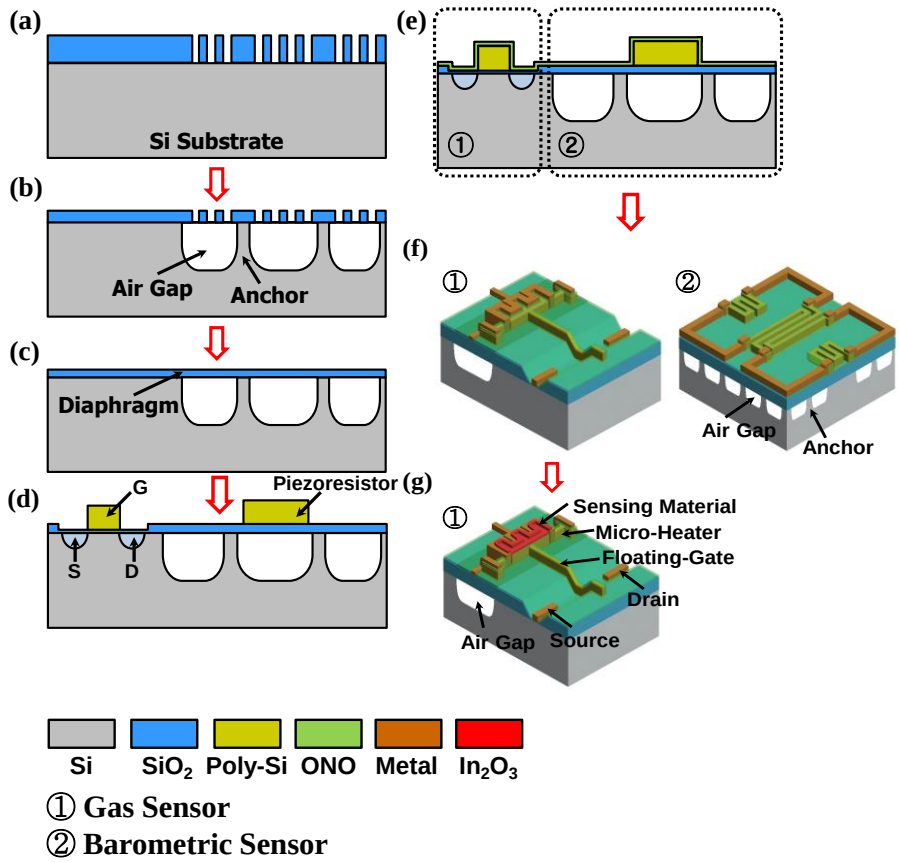

Fig. 2.7 (a)-(g) Schematic views of the key fabrication process steps.

Isotropic etching process is performed to etch Si substrate by using Sulfur Hexafluoride (SF_6) gas through 0.5 μm diameter SiO_2 etching-holes. Through the isotropic etching process, cavities with a depth of 2.5 μm are formed under SiO_2

etching-holes (Fig. 2.7 (b)). The formed cavities become the cavity that can detect the pressure difference from the ambient air pressure of the barometric pressure sensors, and become air-gaps that can maintain the proper operating temperature of the FET-type gas sensors. Since the thermal conductivity of air (0.026 W/(m·K)) is much smaller than that of Si (148 W/(m·K)) or SiO_2 (0.026 W/(m·K)), the air-gap formed in the cavity helps maintain the temperature in the high-temperature operation of the FET-type gas sensors [26]. Since SiO_2 layer is hardly etched during isotropic etching process using SF_6 gas, pillar-shaped Si is left below the 3 × 3 μm^2 square SiO_2 patterns as shown in Fig. 2.10 (b). In this study, these pillar-shaped Si are named anchor. These anchors serve to support the SiO_2 patterns at the top of the cavity. In particular, barometric pressure sensors are designed so that the pressure is concentrated in the central region of the sensor by placing the anchors at regular intervals in all areas including air pockets except the central region of the sensors. Fig. 2.8 shows the depth of the cavity and the shape of the anchor according to the process time of the isotropic etching process using SF_6

gas. Through 2 minutes and 30 seconds process time, a cavity with a depth of 2.5 μm can be formed, and the Si anchor can be made into a shape having a diameter of 1μm.

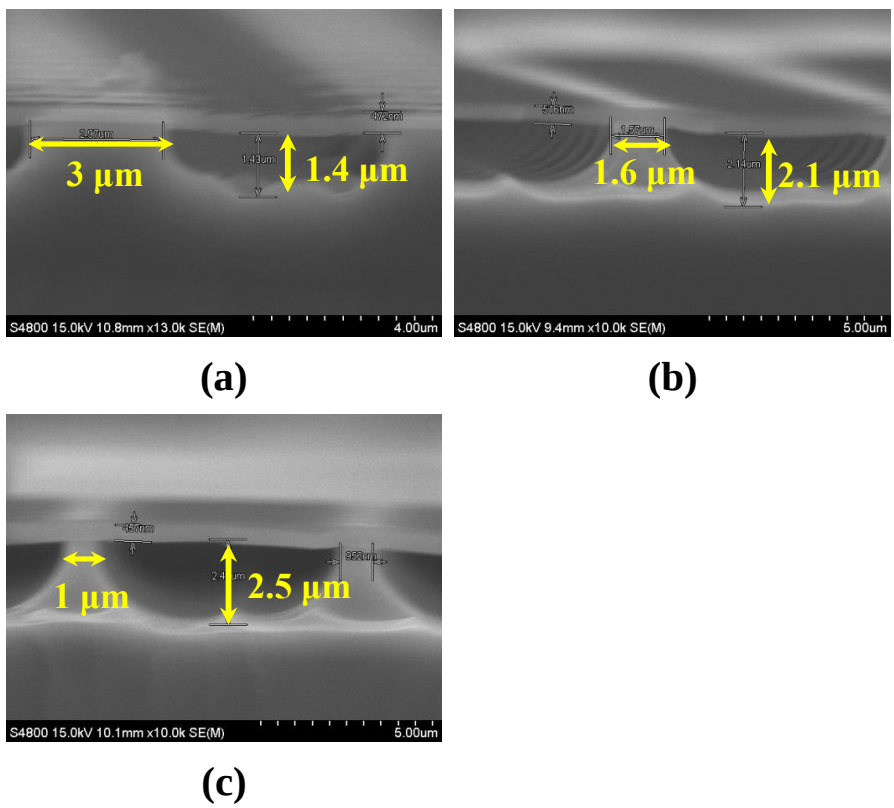

Fig. 2.8 Cross-sectional SEM views according to process time of isotropic etching process using SF_6 gas. (a) 1.5 min, (b) 2.0 min, (c) 2.5 min.

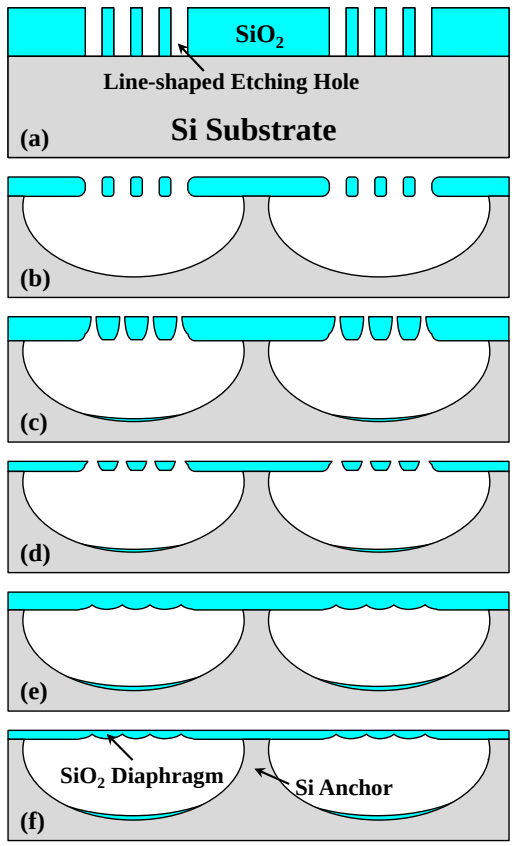

Fig. 2.9 Schematic key process steps for the cavity, (a) patterning of line-shaped etching holes, (b) isotropic etching using SF_6 gas through the etching holes, (c) narrowing the etching holes by depositing PE-TEOS film, (d) anisotropic etch-back process for PE-TEOS film thickness reduction, (e) deposition of another PE-TEOS layer to fully seal the etching holes, (f) etch-back process for thickness reduction of the SiO_2 diaphragm [24].

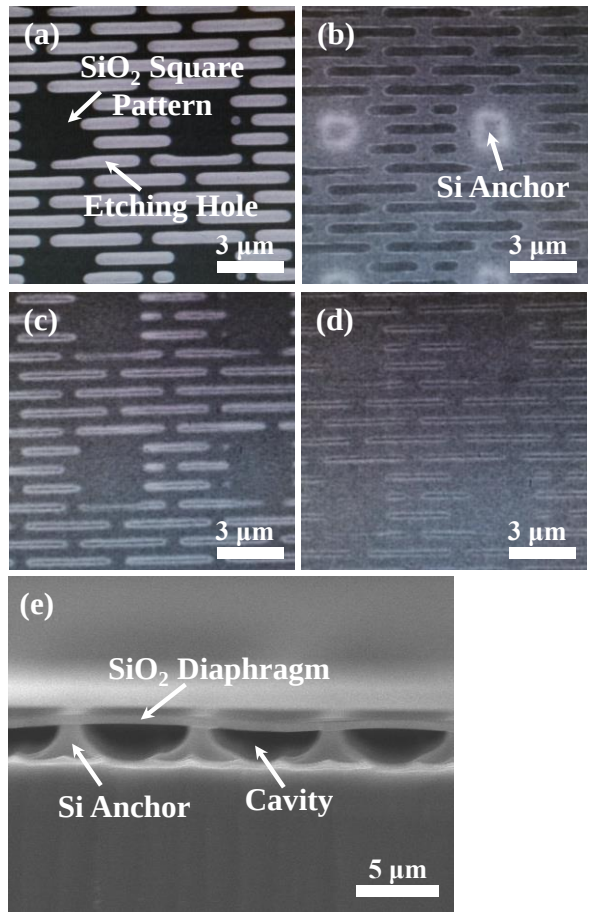

Fig. 2.10 (a) Top SEM view taken after patterning line-shaped etching holes, (b) top SEM view taken after isotropic etching process, (c) top SEM view taken after etch-back process for PE-TEOS layer, (d) top SEM view taken after fully sealing the etching holes, (e) cross-sectional SEM view taken after fully sealing the etching holes [24].

The cavity of the barometric pressure sensor must be sealed to read the pressure difference from outside the cavity. In addition, since the floating-gate and micro-heater of the FET-type gas sensors are formed on the air-gap of the sensors, the cavity must be sealed. The 0.5 μm diameter SiO_2 line-shaped etching holes remain almost the same even after 2.5 minutes of isotropic etching process using SF_6 gas as shown in Fig. 2.10 (b). Fig. 2.9 is schematic diagrams showing the process of sealing line-shaped etching holes. First, Plasma Enhanced Tetraethyl Orthosilicate (PE-TEOS) layer are deposited to reduce the opened diameter of line-shaped etching holes. The PE-TEOS film has a non-conformal profile and can form an over-hang profile to reduce the diameter of the line-shaped etching holes (Fig. 2.9 (c)). Since the deposited PE-TEOS film is very thick, anisotropic etch-back process is used to reduce the deposited thickness of the PE-TEOS film. As shown in the top view of the SEM image Fig. 2.10 (c), the opened diameter of the line-shaped etching hole is reduced (Fig. 2.9 (d)). Once again, PE-TEOS layer is deposited to completely seal the opened line-shaped etching holes (Fig. 2.9 (e),

Fig 2.10 (d)). Then, the anisotropic etch-back process is performed to make the thick PE-TEOS layer thin (Fig. 2.9. (f)). In order to increase the sensitivity of the barometric pressure sensors and increase the heat insulating the FET-type gas sensors, the thickness of the PE-TEOS layer should be reduced as much as possible. However, too thin film has poor mechanical strength, so in this dissertation, the etch-back process is performed to form a film with a thickness of 0.5 μm (Fig. 2.10 (e)). After this etch-back process, the layer formed on the cavity becomes the diaphragm of the barometric pressure sensor. Since the fabricated diaphragm is thin, the barometric pressure sensors have good sensitivity, so the overall size of the sensor can be reduced compared to the conventional MEMS barometric pressure sensors. The SiO_2 diaphragm formed of thermal SiO_2 and PE-TEOS has Young's modulus (66 GPa) and Possion's ratio (0.17) smaller than that of the conventional Si diaphragm (130 GPa, 0.22), so it has good mechanical stability and durability and has more displacement under the same pressure. Table 2.1 compares the key features of the barometric pressure sensors in this

dissertation and the reported literatures [4, 14].

Table 2.1 Comparison of diaphragm thickness, sensor size, and sensitivity between our barometric pressure sensors and reported barometric sensors.

	This study		Reference [4]	Reference [14]
	Normal type	**Air pocket type**		
Diaphragm Thickness (μm)	**0.5**	**0.5**	**3-6**	**3**
Sensor Size (μm^2)	**100×100**	**300×300**	**680×680**	**500×500**
Sensitivity	**2.03 (μV/hPa)**	**2.47 (μV/hPa)**	**30.0 (fF/hPa)**	**0.49 (fF/hPa)**

The next process defined the active region of the MOSFET of the FET-type gas sensors. In order to form a buried channel of the *p*MOSFET, a low dose of BF_2 (Boron-Fluorine) ions are implanted shallowly. A 10nm thick gate-oxide layer is grown on the active region and 0.35 μm thick undoped gate poly-Si layer is subsequently deposited on the gate-oxide layer by Low Pressure Chemical Vaper Deposition (LP-CVD). The poly-Si layer is doped with a high concentration of B

by ion implantation (BF_2, 5×10^{15} cm^{-2}) and annealed at 1050 ºC for 5 seconds and then patterned as FG of the MOSFET, micro-heater of the gas sensors and piezo-resistors of the barometric pressure sensors. The poly-Si with heavily doped has high piezo-resistance, linear Temperature Coefficient of Resistance (TCR) and low depletion effect. These properties allow the poly-Si as the piezo-resistors and temperature sensors of the barometric pressure sensors, the FG of the MOSFET, the micro-heater of the gas sensors at the same time. In this way, the poly-Si becomes a key role of the sensors, enabling efficient integration. To form the source and the drain regions of the MOSFET, B ions with a dose of 2×10^{15} cm^{-2} are implanted (Fig. 2.7 (d)), and then ONO passivation layers are deposited (Fig. 2.7 (e)). Next, the contact holes are defined by photo lithography (4th photo mask) and anisotropic etching process. After performing photo lithography process for the metal line (5th photo mask), Chrome (Cr) (30 nm) and Gold (Au) (50 nm) layers are deposited by sputtering process, and then metal line is formed by lift-off process (Fig. 2.7 (f)). In order to improve the contact characteristics and the

subthreshold swing characteristics of the MOSFETs, the anneal process is carried out for 30 minutes in a hydrogen atmosphere at 300 ºC. Finally, 12 nm thick *n*-type semiconducting In_2O_3 layer is formed around CG and FG as a sensing material (Fig. 2.7 (g)).

2.4.2. Formation of sensing material on FET-type gas sensors

In the FET-type gas sensor, the CG and the FG are separated, and the sensing layer is filled between them. Fig. 2.5 (a) is the top view SEM image of the fabricated FET-type gas sensor. As shown in Fig. 2.5 (a), the sensing layer is formed between the CG and the FG. The sensing layer reacts directly with target gas to change the potential delivered to the FG, affecting the V_{th} or I_D of the FET of the gas sensors. Fig. 2.5 (b) is a schematic cross-sectional view of the FET-type gas sensors. As shown in Fig. 2.5 (b), the CG and the In_2O_3 layer are in contact, and the FG and the In_2O_3 layer are separated by ONO layers. As the sensing materials, meta oxides, carbon materials, 2D dichalcogenides are reported. In this study, In_2O_3 with *n*-type semiconducting characteristics is used as the sensing layer. After patterning the space between the FG and the CG by photolithography (6th photomask), In_2O_3 layer with 12 nm thickness is deposited by Radio Frequency (RF) sputtering and Photo Resist (PR) is removed by lift-off process. Fig. 2.11 (a) is the magnified top view SEM image of the deposited In_2O_3 film and Fig. 2.11 (b)

is an Energy Dispersive X-ray Spectroscopy (EDS) analysis of the In_2O_3 layer used as the sensing layer of the FET-type gas sensors. By using EDS analysis, we observed the In (Indium) peak at 3.444 keV and 3.487 keV.

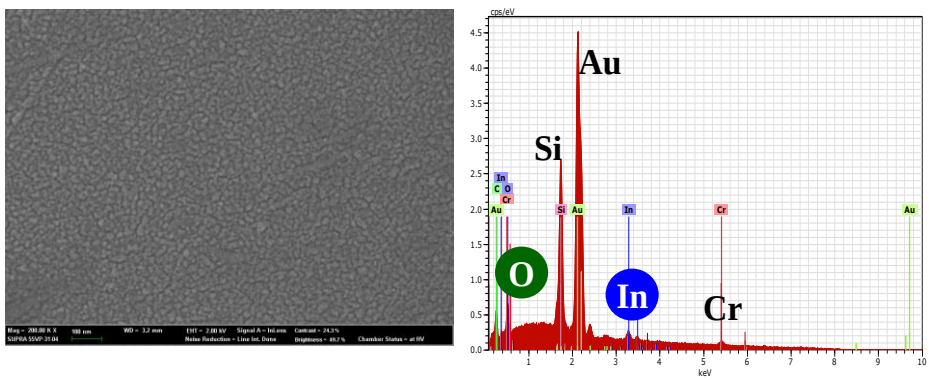

(a) **(b)**

Fig. 2.11 (a) Magnified top view SEM image of deposited In_2O_3 film, (b) EDS analysis of In_2O_3 layer used as sensing layer of FET-type gas sensors.

Chapter 3. Device characteristics

3.1. Characteristics of barometric pressure sensors

3.1.1. Device simulation

COMSOL Multiphysics (version 5.3) is used to confirm the characteristics of the barometric pressure sensors fabricated in this dissertation [28]. The physics used in the simulation are 'Solid Mechanics'. The behaviors of the diaphragm of the barometric pressure sensors are verified using COMSOL Multiphysics. Using the solid mechanics physics, the displacement and profile of the diaphragm according to changes in air pressure are verified.

Fig. 3.1 shows models designed using COMSOL Multiphysics. All models are designed in 3-dimensions and implemented in the same way as actual fabricated materials. Four types of barometric pressure sensors are proposed and

fabricated. Models with the same physical size as the barometric pressure sensors are designed. There are types of barometric pressure sensors having conventional piezo-resistors with no air pockets, and conventional piezo-resistors with air pockets. In addition, there are types of barometric sensors having newly proposed piezo-resistors with no air pockets, and sensors having newly proposed piezo-resistors with air pockets. In addition, the difference in volume inside the cavity according to the presence or absence of the air pocket is reflected.

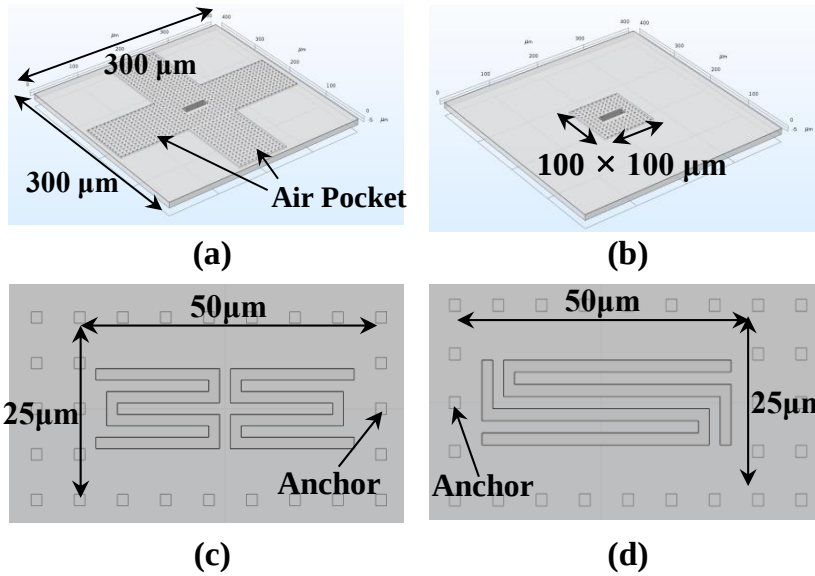

Fig. 3.1 Barometric sensors (a) air pocket type and (b) normal type models, and patterns of (c) conventional and (d) proposed piezoresistors models designed by COMSOL Multiphysics [28].

Each designed barometric pressure sensor model has a 10 µm thick *p*-type Si substrate with a 2.5 µm deep cavity and a 0.5 µm thick SiO_2 diaphragm. Si anchors are arranged at regular intervals like the actually fabricated sensors, and heavily *p*-doped poly-Si piezo-resistors are placed on the SiO_2 diaphragm. Fig. 3.2 shows the simulation result after implantation 5×10^{15} cm^{-2} dose of BF_2 ions into

undoped poly-Si with an energy of 90 keV, and then carried out Rapid Temperature Annealing (RTA) for 5 seconds at 1050 ºC. The simulation is performed using Synopsys Inc. Sentaurus [59]. The *p*-type poly-Si used as piezo-resistors are set at a concentration of 2.1×10^{20} cm^{-3}, and this concentration is the result of the simulation. Metal wirings and probing pads are omitted because those factors are hardly effective on the simulation.

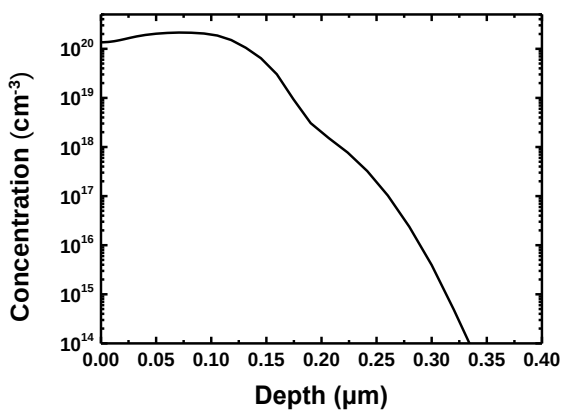

Fig. 3.2 Simulation result after implantation BF_2 ions (5×10^{15} $cm^{-2,}$ 90 keV) into undoped 0.35 μm thick poly-Si and then RTA (5*s*, 1050 ºC) [59].

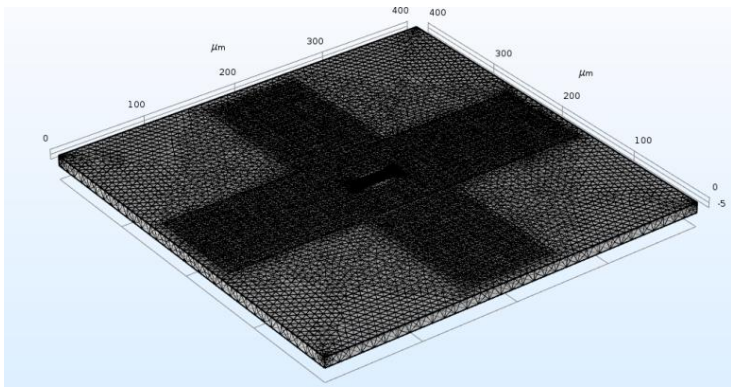

Fig. 3.3 Model of air pocket type barometric pressure sensor with tetrahedral mesh.

As shown in Fig. 3.3, tetrahedral mesh is built in the entire area of the models, and more dense mesh is built in the central region of the diaphragm and piezo-resistors where the pressure is applied. And the pressure according to the pressure difference is set to be applied to the upper part of the diaphragm. While changing the ambient pressure from 100 hPa to 1013 hPa, the displacement and profile of the diaphragm, and the resistance change of the piezo-resistor are confirmed.

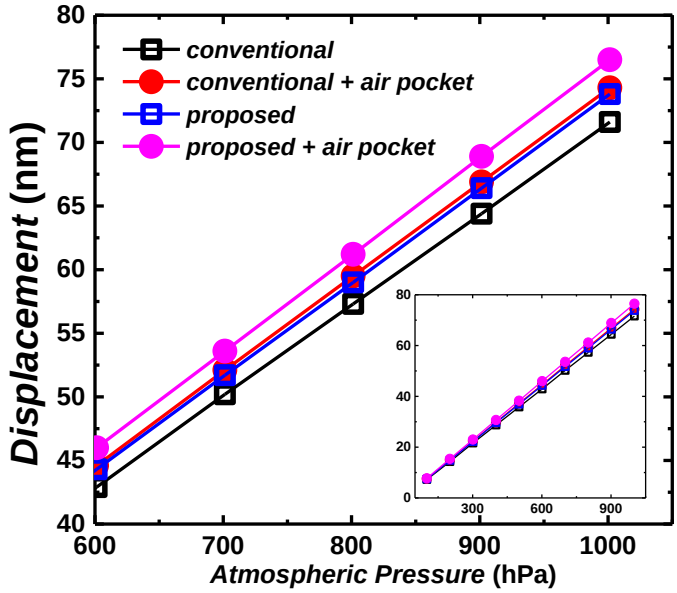

Fig. 3.4 Diaphragm displacement obtained by simulating the structures and patterns shown in Fig. 3.2 using COMSOL Multiphysics.

Fig. 3.4 is curves showing the displacement of the diaphragm according to the change in atmospheric pressure in each model. It can be shown that barometric pressure sensors having air pockets have a larger displacement than sensors not having air pockets. In the sensors having piezo-resistor of the same design, the displacement of the diaphragm is up to 5 nm depending on the presence or absence

of the air pockets. As confirmed by Boyle's Law,

$$P_1V_1 = P_2V_2 \tag{3}$$

it is confirmed that the increased total volume of the cavity due to the air pockets resulted in an increase in pressure applied to the central region of the diaphragm. Fig. 3.5 shows the profile of the diaphragm deformation according to the design of the piezo-resistor. The diaphragm deformation of newly proposed piezo-resistor shows more gradual curvature than conventional piezo-resistor type. As shown in this way, since it shows a gradual curvature over the entire area of the piezo-resistor, it has a more positive influence on the change in piezo-resistance.

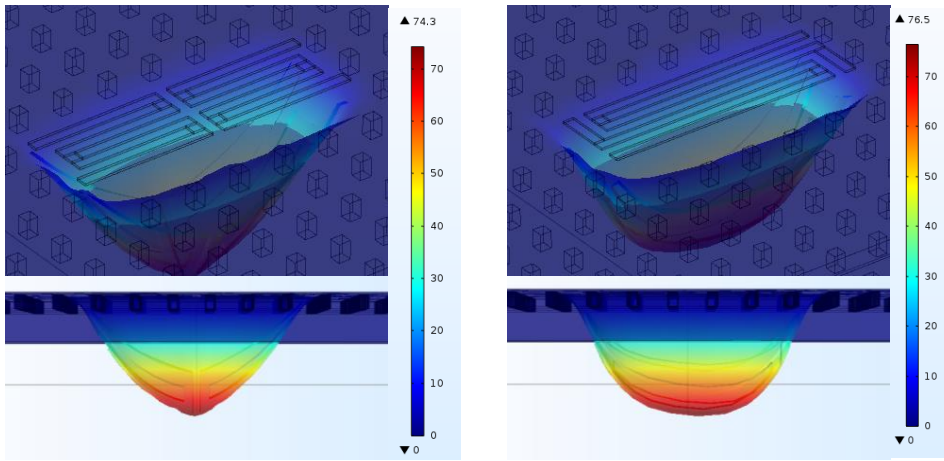

(a) **(b)**

Fig. 3.5 Displacement profiles of (a) the conventional piezoresistors patterns and (b) the proposed pattern at a given pressure of 1013 hPa.

3.1.2. Measurement setup

Fig. 3.6 shows the experimental setup for measuring barometric pressure sensors and FET-type gas sensors on the same chip. The measurements are carried out by using a vacuum chamber with probe station. And this measurement system equipped with Baratron gauge, pressure controller, Mass Flow Controller (MFC) system, mixing chamber, gas cylinders and temperature controller. Below the

probe station, there Is the heater that can raise the temperature, and it can be adjusted from room temperature to 250 ºC by using temperature controller. The measurement chamber can set a specific pressure using the pressure controller. The pressure controller reads the pressure of the chamber through the Baratron gauge and controls the throttle valve connected to the rotary pump and the MFC system connected to the dry air cylinder to set a specific pressure. In this way, the characteristics of the barometric pressure sensors can be confirmed by setting a specific pressure and temperature in the measurement system. In particular, the barometric pressure sensors have a built-in temperature sensor and can measure temperature and atmospheric pressure at the same time.

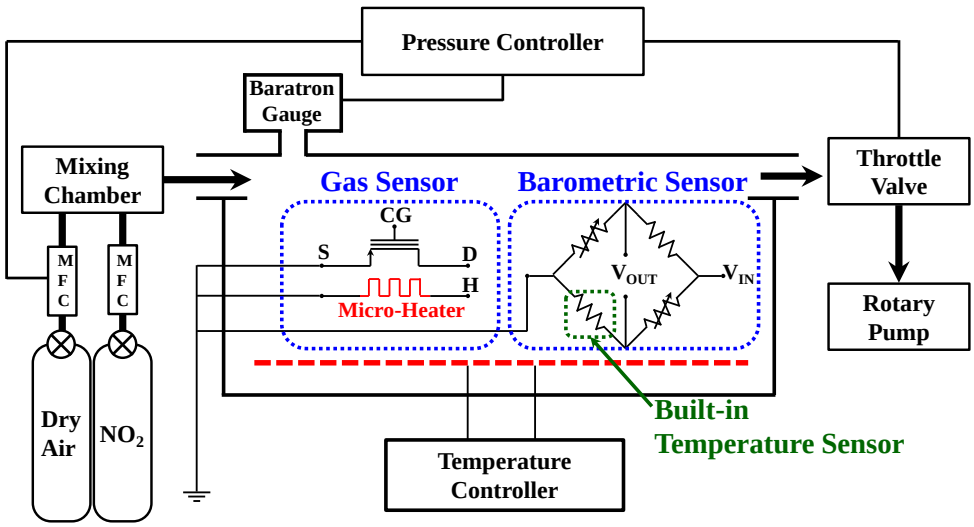

Fig. 3.6 Experimental setup for atmospheric pressure measurement and gas sensing measurement.

In this study, the characteristics of the FET-type gas sensors are investigated using NO_2 gas as the target gas. In order to make a specific ratio of NO_2 gas, the flow rate of dry air and NO_2 gas are controlled by MFC, then mixed in a mixing chamber and injected into the measurement chamber.

3.1.3. Measurement results

As shown in Fig. 2.4, the barometric pressure sensors have two fixed piezo-resistors and two variable piezo-resistors, and since the variable piezo-resistors are placed on the diaphragm that is deformed according to the atmospheric pressure, the piezo-resistance value of the variable piezo-resistors changes depending on the atmospheric pressure. Fig. 3.7 (a) shows the piezo-resistance change (ΔR_{piezo}) of the variable piezo-resistor according to the change in air pressure of the fabricated barometric pressure sensors. The difference in sensitivity of piezo-resistance can be confirmed depending on the presence or absence of the air pockets. In addition, the barometric pressure sensor with newly proposed piezo-resistors has a larger ΔR_{piezo} than the barometric pressure sensor with conventional piezo-resistors. Fig. 3.7 (b) are curves showing the output voltage (ΔV_{out}) of the barometric pressure sensors according to the change in air pressure. It can be seen that the sensitivity of the barometric pressure sensor with

the newly proposed piezo-resistors and air pockets is the best. Table 2.1 shows the sensor size, the diaphragm thickness and the sensitivity of the reported barometric pressure sensors. Compared with reported sensors, the barometric pressure sensor fabricated in this work has a small size. This is because the barometric pressure sensor has a thin diaphragm, newly proposed piezo-resistor and air pockets that can increase sensitivity of the sensor, reducing the overall size of the sensor.

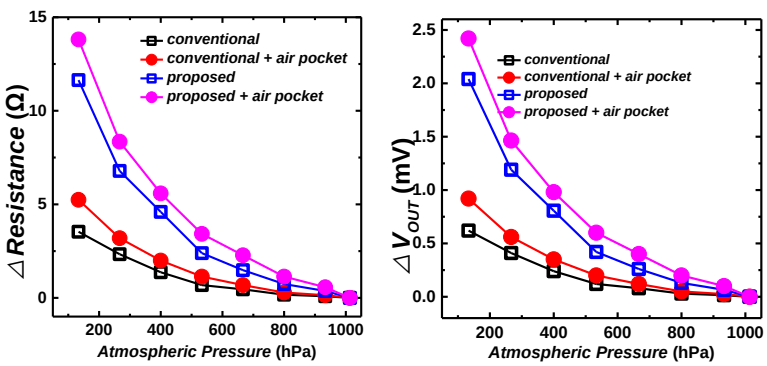

Fig. 3.7 (a) Measured piezoresistance change (ΔR_{piezo}) and (b) output voltage change (ΔV_{out}) of Wheatstone bridge circuit with the atmospheric pressure change.

Fig. 3.8 (a) shows the change in ΔV_{out} of the barometric pressure sensors according to the change in ambient temperature (T). As the T increases, the sensitivity of the barometric sensor decreases because the sensitivity of poly-Si piezoresistor decreases [10, 18, 19].

Fig. 3.8 (b) shows the results of the repeated measurement of the barometric pressure sensor with newly proposed piezo-resistor and air pockets. More than 100 measurements are carried out at atmospheric pressure of 133 hPa, 266 hPa and 666 hPa, respectively, and stable results are obtained even repeated measurements. Since Young's modulus (66 GPa) and Poisson's ratio (0.17) of the SiO_2 diaphragm are smaller than Si (130 GPa, 0.22), mechanical strength and durability of the SiO_2 diaphragm are guaranteed even after repeated measurements.

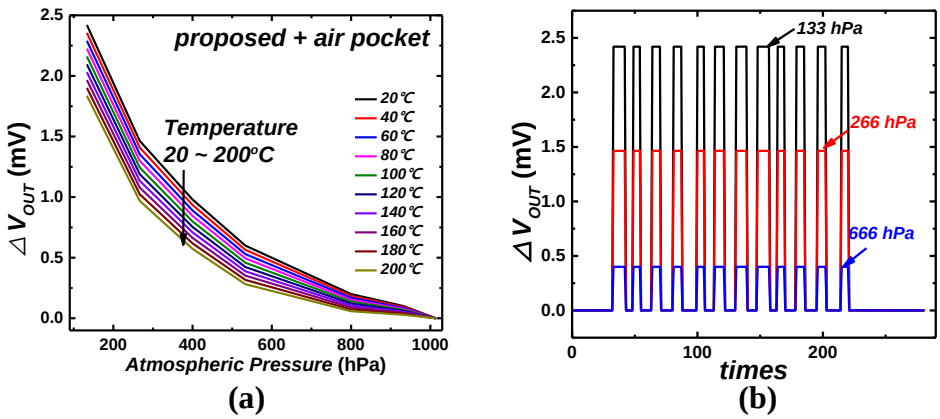

Fig. 3.8 (a) Measured output voltage (ΔV_{out}) change of the barometric sensor with atmospheric pressure as a parameter of ambient temperature. (b) Repeated pressure measurement of the barometric sensor.

3.2. Characteristics of temperature sensors and micro-heater

3.2.1. Temperature sensor and its characteristics

Fig. 3.9 is a top view SEM image of the temperature sensor built into the barometric pressure sensors. The poly-Si electrode used as the fixed piezo-resistors of the barometric pressure sensors can be operated as the temperature sensors [26]. The poly-Si electrode become the piezo-resistors of the barometric pressure sensors, and function as an electrode of the temperature sensor as well. It can read the resistance of the poly-Si by setting the read voltage in one direction of the poly-Si electrode and grounding in the other direction of the electrode. By reading the resistance of the poly-Si electrode, the ambient temperature can be calculated. In this study, the temperature of the substrate where the sensors are fabricated is controlled using the temperature controller in the measurement chamber and the resistance value of the temperature sensor is checked.

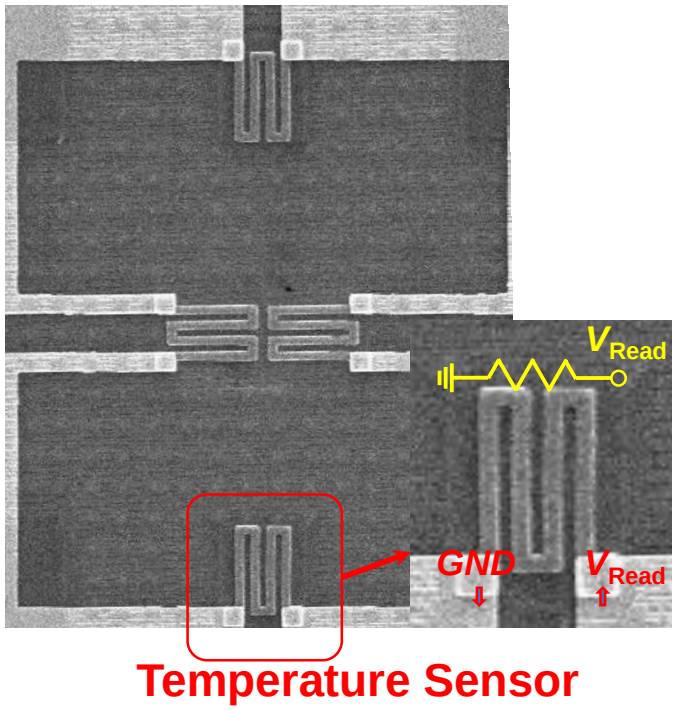

Fig. 3.9 Top view SEM image of temperature sensor built-in barometric pressure sensor.

$$R\,(T) = R_0\,[1 + \alpha\,(T - T_0)] \quad (4)$$

Eq. (4) shows the correlation between the temperature and the resistance. α is called TCR. TCR is the calculation of a relative change of resistance per degree of temperature change. Fig. 3.10 shows the TCR according to the dose of Boron

ion implanted into the 350 nm thick poly-Si. Using the temperature controller, the temperature from -20 ºC to 200 ºC is set and the resistance of poly-Si is measured. When low dose of Boron is implanted, poly-Si showed negative TCR at low temperature regions and positive TCR at high temperature regions. Since it has a U-shaped TCR, it is difficult to trace the temperature depending on the resistance. As the dose of Boron implanted into poly-Si increases, poly-Si has a more linearly positive TCR. In this study, heavy dose of 5×10^{15} cm^{-2} is implanted into the undoped poly-Si, and this implanted poly-Si shows linear TCR of 2.4×10^{-4}. In addition, it has almost linear TCR from -20 ºC to 200 ºC, so it is easy to trace back the temperature by reading the resistance of the poly-Si electrode.

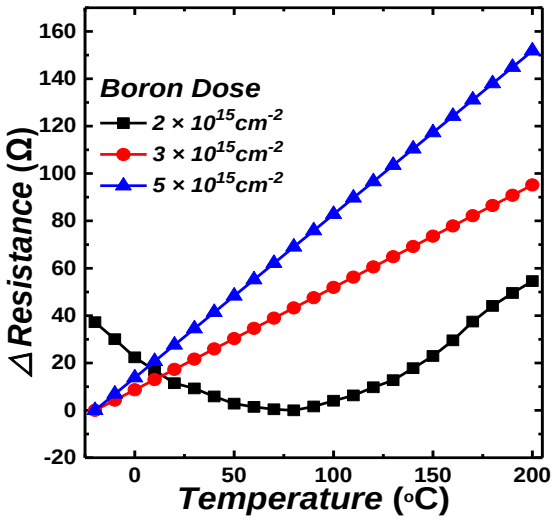

Fig. 3.10 Resistance change with temperature as a parameter of implanted boron dose into 350nm poly-Si.

Fig. 3.11 shows the correlation between the ambient temperature and the resistance according to the applied voltage of the temperature sensor. As the reading voltage (V_r) is increased, the resistance is rapidly increased by Joule heating above 150 ºC. V_r below 1V shows a nearly linear TCR. In this study, the ambient temperature is measured using a reading voltage of 0.5 V, so that Joule heating is almost ignored.

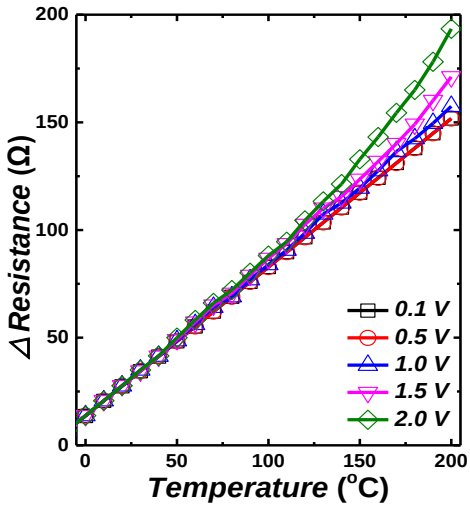

Fig. 3.11 Resistance change with temperature as a parameter of read voltage.

The accuracy of the temperature sensor is verified using Infra-Red (IR) thermal microscopy. A chip with fabricated temperature sensor is placed on a Peltier device capable of temperature control by Proportional Integral Differential (PID) controller, and the temperature of the Resistance Temperature Detector (RTD) sensor and IR thermal microscopy are simultaneously checked. Also, the resistance change of the fabricated temperature sensor is observed. Fig. 3.12 (a) is

the overall picture of the system used for verification, and Fig. 3.12 (b) is the picture of the sample used for measurement. Fig. 3.13 shows that the difference between temperature controlled by the PID controller and the temperature confirmed by the IR thermal microscopy is less than 2 ºC. Also, the linear change in resistance change due to the temperature change is confirmed. Therefore, by checking the resistance value of the temperature sensor, it is possible to track the ambient temperature. In this study, it is verified that a 350 nm thick undoped poly-Si is implanted with a heavy dose of Boron ions to operate as a temperature sensor.

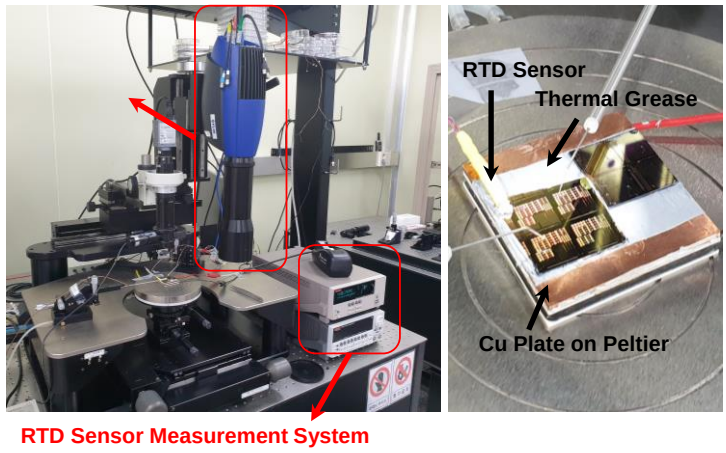

Fig. 3.12 (a) Overall picture of the system used for verification, (b) picture of the sample used for measurement.

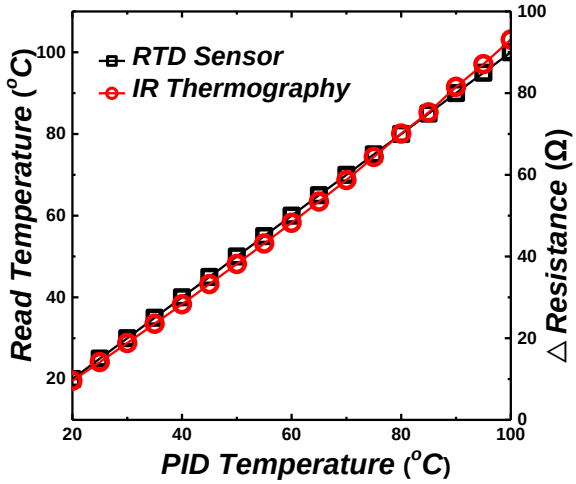

Fig. 3.13 Temperature confirmed by IR thermal microscopy and RTD sensor.

3.2.2. Micro-heater of the gas sensors

In order to detect various kinds of target gases, it is necessary to make an appropriate ambient temperature for each gas detection [26]. In this dissertation, a gas sensor for detecting NO_2 gas is fabricated, and the proper temperature for detecting NO_2 gas is around 150 ºC. The air-gap and localized micro-heater are used to maintain high operating temperature for detecting NO_2 gas. Fig. 2.5 (a) is the top view image of the fabricated gas sensor. The micro-heater made of 350 nm thick poly-Si surrounds the FG and the sensing material. The heating area is 27 × 7 μm^2. The gas sensor has low power consumption because the micro-heater heats only the area required for gas detection. Fig. 3.14 (a) shows the *I-V* curve of the fabricated micro-heater of the gas sensors. The micro-heater fabricated in this dissertation shows a power consumption of 3.85 mW at a temperature of 124 ºC, and has a lower power consumption than other reported heaters.

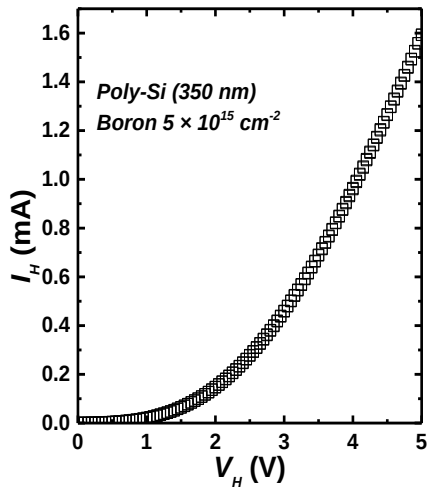

Fig. 3.14 *I-V* curve of the fabricated micro-heater.

The air-gap formed under the micro-heater prevents heat dissipation. Si has high thermal conductivity (130 W/m·K), and air has very low thermal conductivity (0.026 W/m·K), so the air-gap efficiently prevents heat dissipation from the micro-heater. And the air-gap prevents the heat of the micro-heater from spreading to the channel of the MOSFET, which ensures stable operation of the MOSFET. Thanks to the localized micro-heater and the air-gap, only the temperature of the sensing material for sensing NO_2 gas can be increased.

The micro-heater is simulated using COMSOL Multiphysics to verify the behaviors of the micro-heater according to the heater bias voltage (V_H). The physics used in the simulation are 'Electric Current', 'Heat Transfer in Solid' and 'Heat Transfer in Fluids'. The simulation model with the same physical structure as the fabricated gas sensor is designed (Fig. 3.15 (a)) and a dense mesh is applied as shown in Fig 3.15 (b). The model has the air-gap with 2.5 μm depth, and the outside of the sensor is covered with air. The Substrate under the model and the air top are set at 25 ºC.

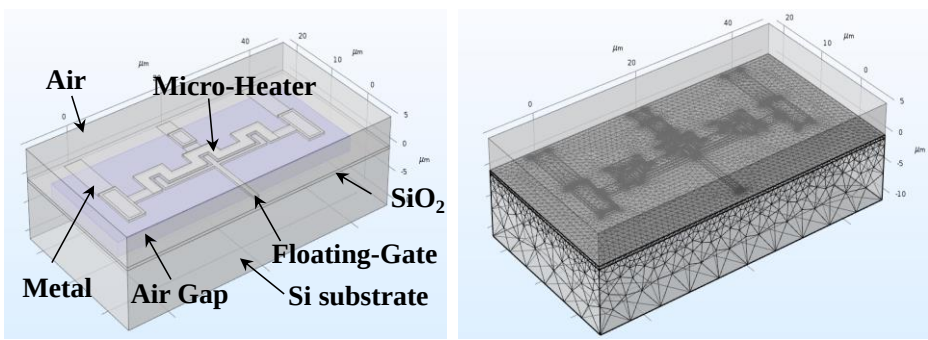

Fig. 3.15 (a) Structure of micro-heater for simulation and (b) its mesh profile.

Fig. 3.16 shows the simulation results of COMSOL Multiphysics and the results of IR thermal microscopy. As shown in Fig. 3.16, the simulation results and the temperature confirmed by IR thermal microscopy are almost identical. Fig. 3.17 (a) shows the temperature distribution of the simulation model at 4 V of V_H. Around the micro-heater has a temperature (T_H) of 124 ºC, and heat preservation by the air-gap is confirmed. Fig. 3.17 (b) shows the 3D temperature distribution and confirms that heat dissipation is prevented due to the air-gap under the micro-heater. Fig. 3.18 is the temperature distribution data of the fabricated gas sensor when V_H is 4 V by using Thermo-Reflectance Microscopy. It shows almost same result as the temperature distribution of the simulated model. And it is confirmed that no temperature increase is observed in the vicinity of the MOSFET.

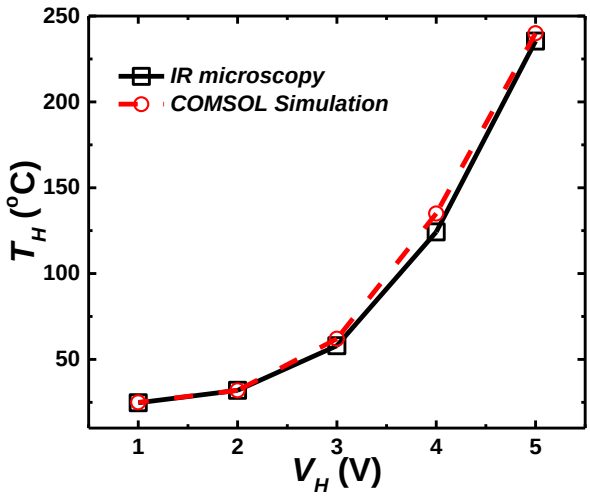

Fig. 3.16 simulation results of COMSOL Multiphysics and the results of IR thermal microscopy.

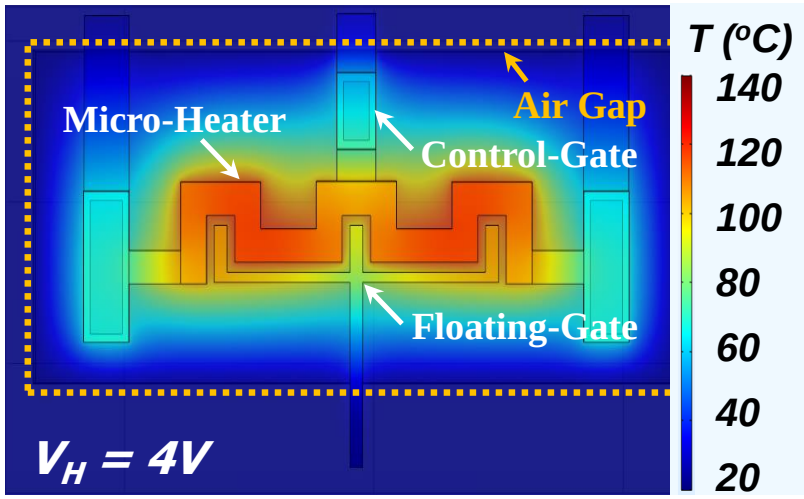

(a)

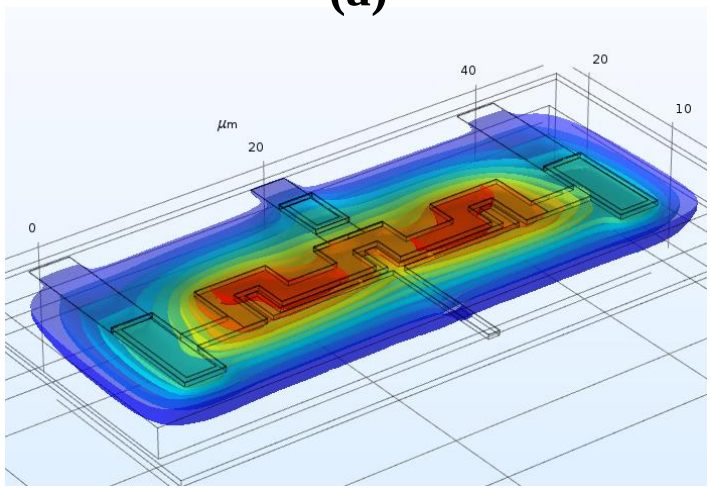

(b)

Fig. 3.17 (a) simulated temperature distribution and (b) 3D temperature distribution when V_H is 4 V by using COMSOL Multiphysics.

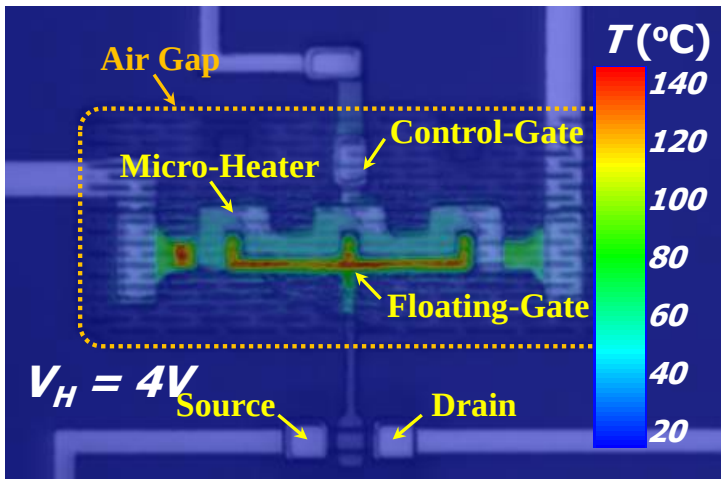

Fig. 3.18 Temperature distribution image obtained by the thermo-reflectance microscopy of the gas sensor when V_H is 4 V.

3.3. Characteristics of gas sensors

3.3.1. *I-V* characteristics and nonvolatile functionality of FET-type gas sensors

Fig. 3.19 (a) shows curves showing I_D according to the CG bias (V_{GS}) of FET-type gas sensors, and Fig. 3.19 (b) is curves showing the I_D according to the drain voltage (V_{DS}). From these curves, reasonable operating characteristics of *p*MOSFET are verified. Fig. 3.19 (c) shows I_D versus the V_{GS} curves of FET-type gas sensors. Since the horizontal FG of the gas sensor is made of the poly-Si with nonvolatile functionality, the V_{th} of the sensors can be adjusted by applying program bias (V_{PGM}) or erase bias (V_{ERS}). In this way, since the V_{th} of the fabricated gas sensors can be modified, high-quality gas sensors can be mass-produced.

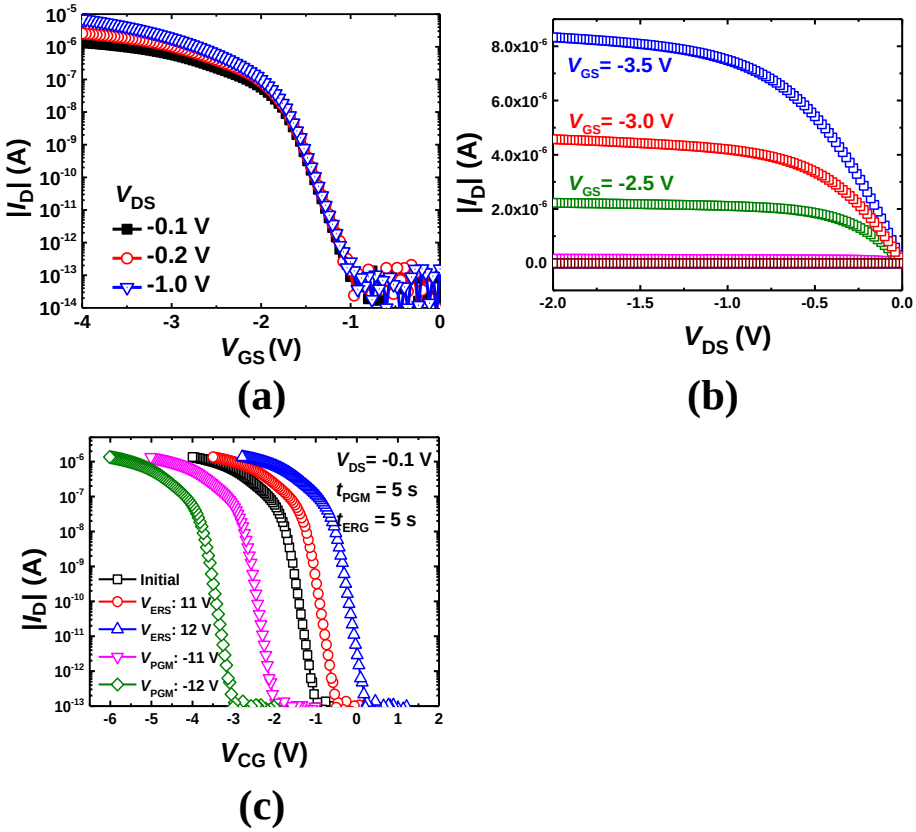

Fig. 3.19 (a) I_D versus V_{GS} curves as a parameter of V_{DS} and (b) I_D versus V_{DS} curves of as a parameter of V_{GS} of a *p*MOSFET. (c) I_D versus V_{GS} curves of a *p*MOSFET with horizontal FG as parameters of V_{PGM} and V_{ERS}.

3.3.2. Gas sensing mechanism

Fig. 3.20 shows the equivalent circuit of the FET-type gas sensor. The capacitance of In_2O_3 layer used as the sensing material is denoted as C_{InO}, and the capacitance of the ONO passivation layer protecting the FG is denoted as C_{ONO}, respectively. C_G and C_P represent the gate oxide capacitance of the MOSFET and parasitic capacitance of the gas sensor, respectively. The coupling ratio (γ) between the CG and the FG can be obtained as follows.

$$\gamma = \frac{(C_{InO}^{-1} + C_{ONO})^{-1}}{(C_{InO}^{-1} + C_{ONO})^{-1} + C_P + C_G} \quad (5)$$

When the sensing material reacts with target gas in Eq. (5), C_{InO} changes and eventually γ changes. The voltage delivered to the gate of MOSFET changes depending on the change in γ. Eq. (6) shows the I_D in the linear region of the *p*MOSFET. When the target gas reacts with the sensing material, γ and V_{th} are changed, and finally I_D is changed.

$$I_D = -\mu C_g \frac{W}{L}(|\gamma V_{GS} - V_{th}| + \frac{1}{2}V_{DS})V_{DS} \quad (6)$$

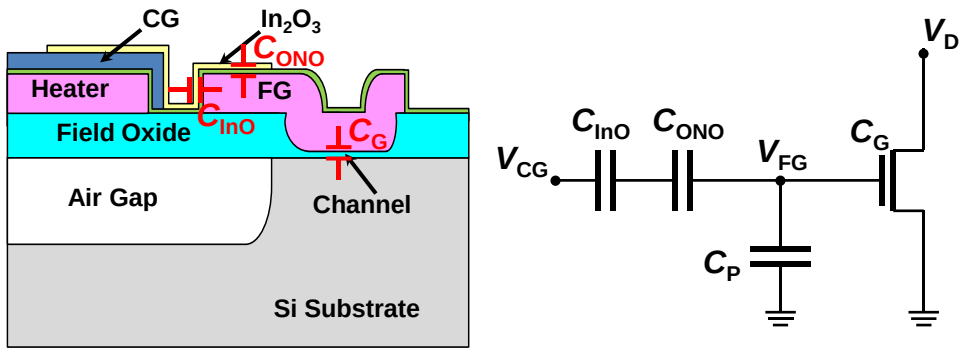

Fig. 3.20 equivalent circuit of the FET-type gas sensor.

Fig. 3.21 is a schematic energy band diagram of the FET-type gas sensor in flat band condition. Φ_{CG}, Φ_{InO}, Φ_{FG}, and Φ_{Si} represent work functions of the CG, the In_2O_3 layer, the FG, and the Si, respectively. The work function of gold (Au) used as the CG in this study has a value of 5.1 eV, and Φ_{InO} is 5.0 eV. Also, Φ_{FG} is ~ 4.05 eV and Φ_{Si} is ~4.26 eV. χ_{InO} and χ_{Si} represent electron affinities of the In_2O_3 layer and the Si, respectively.

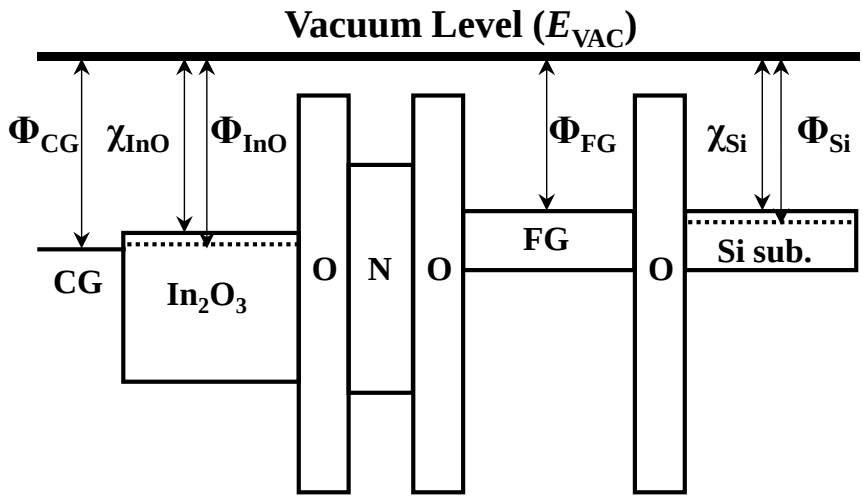

Fig. 3.21 schematic energy band diagram of the FET-type gas sensor in flat band condition.

Fig. 3.22 shows a schematic energy band diagram of the FET-type gas sensor when exposed to NO_2 gas used as the target gas in this study. When the In_2O_3 layer is exposed to NO_2 gas, NO_2 molecules are extracted as electrons from In_2O_3 and adsorbed on the surface of In_2O_3 to exist as negative ions (NO_2^-). As shown in Fig. 3.22 (b), this reaction increases the hole concentration of the Si substrate by increasing the depletion width and band bending ($\psi_{s1} < \psi_{s2}$). As a result, these changes cause changes in V_{th} and I_D.

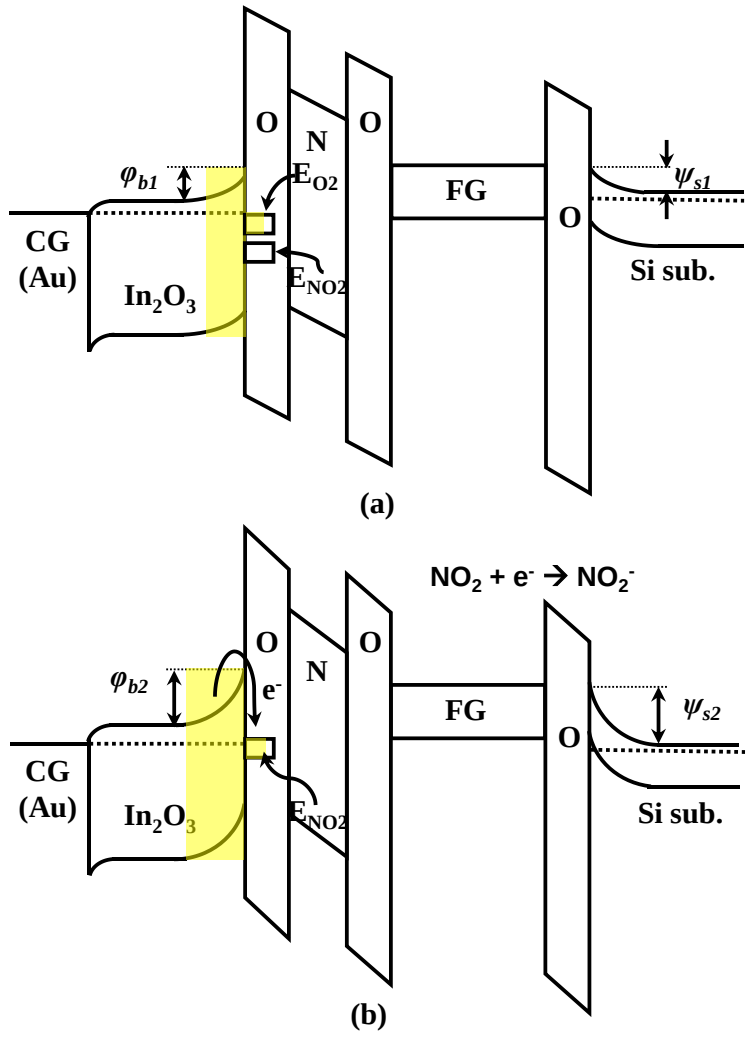

Fig. 3.22 a schematic energy band diagram of the FET-type gas sensor

(a) before adsorption and (b) after adsorption when exposed to NO_2 gas.

3.3.3. Gas measurement results

FET-type gas sensor fabricated in this dissertation is measured on the target gas of NO_2. To react NO_2 gas, the micro-heater built into the gas sensor is used, and T_H is measured with the temperature sensor. Table 3.1 shows T_H of the gas sensor according to V_H. Fig. 3.23 shows the reaction of the gas sensor according to V_H applied to the micro-heater. As V_H increases the response characteristic is improved in the ambience of 1.25 ppm NO_2 gas due to increasing T_H. It is possible to detect NO_2 gas of 1.25 ppm above 3 V at V_H, and it shows high sensitivity at 4 V.

Table 3.1 T_H of the gas sensor according to V_H.

V_H (V)	T_H (°C)
0	**25**
1.0	**25**
2.0	**36**
3.0	**62**
4.0	**124**

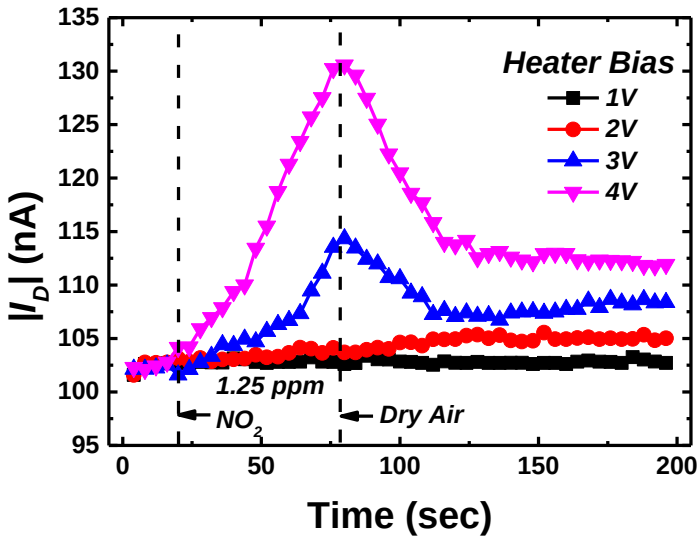

Fig. 3.23 Transient I_D behaviors of the gas sensor as a parameter of V_H. 1.25 ppm of NO_2 gas and dry air are injected at t=25 s and t=75 s, respectively.

Fig. 3.24 shows the graph of detecting NO_2 gas of 0.5 ~ 1.25 ppm when 4 V is applied to V_H. As shown in Fig. 3.24, it is possible to detect NO_2 gas at a very low concentration of 0.5 ppm.

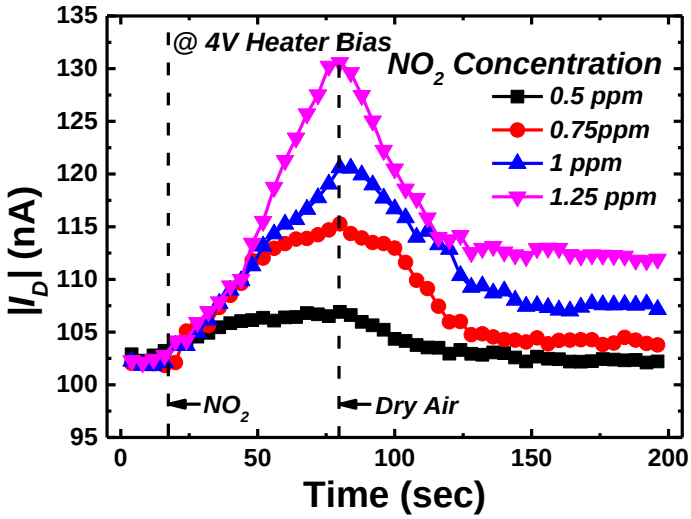

Fig. 3.24 Transient I_D behaviors of the gas sensor with different NO_2 concentrations. NO_2 gas and dry air are injected at t = 25 s and t = 75 s, respectively.

3.4. MLP neural network

As shown in Fig. 3.8 (a), the sensitivity of the barometric pressure sensor decreases as the ambient temperature increases. This is because the characteristics of piezo-resistance become insensitive as the temperature increases. Therefore, it is difficult to measure the exact atmospheric pressure according to the ambient temperature. In this dissertation, since the barometric pressure sensor with built-in temperature sensor is fabricated, it is possible to measure the temperature and the atmospheric pressure at the same time. In order to reduce the error due to the ambient temperature, Multi-Layer Perceptron (MLP) with one hidden layer (12 neurons) is designed as a neural network to provide an exact pressure regardless of ambient temperature. The input of the network is the V_{out} of the barometric sensor and resistance (R_{temp}) of the temperature sensor, and the output is the accurate pressure as shown in Fig. 3.25. The (25 × 19) training data are 25 different pressures measured at each of 19 different Ts (20 ~ 200 ºC).

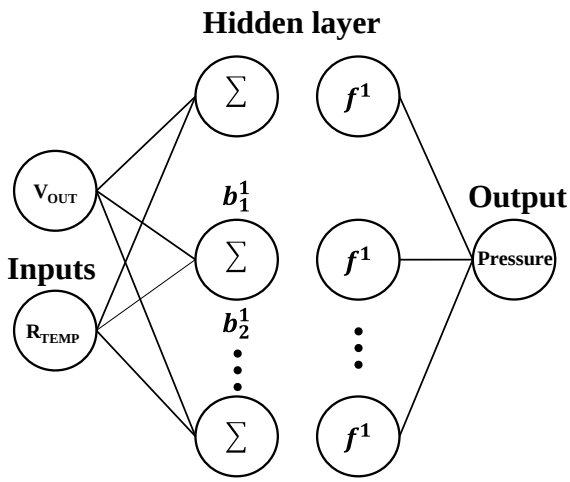

Fig. 3.25 MLP neural network with one hidden layer used for inferencing the pressure of the barometric sensor regardless of temperature change.

The amount of data is increased 1000 times by data augmentation using the repeated measurement data shown in Fig. 3.26 (a). The 5 × 19 test data are 5 different pressures measured at each of the 19 different *T*s, which is different from the training data. Mean Squared Error (MSE) is used as a loss function and back propagation algorithm is used for training. The rectified linear unit is used as an activation function in the hidden layer. Fig. 3. 26 (b) shows that the pressure can

be read with an accuracy of 97.5 % even in a *T* changing environment.

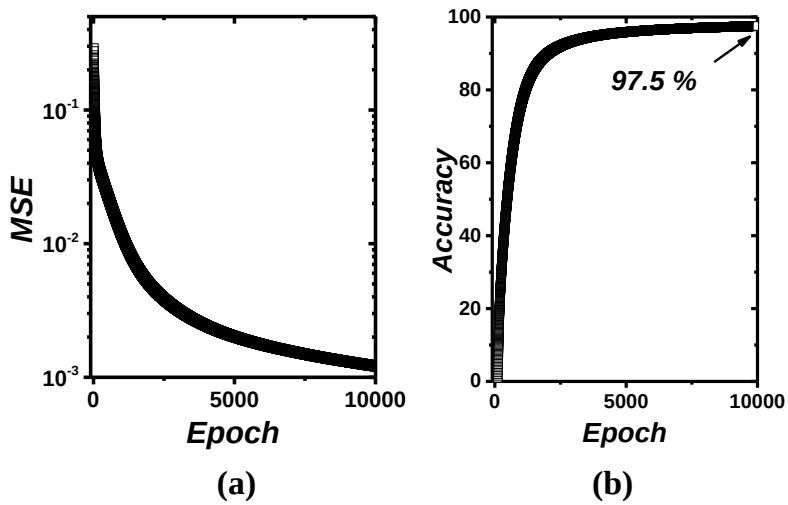

Fig. 3.26 (a) MSE and (b) Accuracy of the test data versus epoch. The accuracy is 97.5 %.

Chapter 4. Conclusion

In this dissertation, efficient integration of barometric pressure sensors and FET-type gas sensors has been proposed and fabricated on the same substrate using conventional CMOS process technology. The cavity and heavily doped poly-Si are designed to be key components for efficient sensor integration. The 2.5 μm deep cavities formed by isotropic etching process by SF_6 gas through SiO_2 etching holes are not only used as the air-gap of the gas sensors to maintain the operating temperature but also used as the cavity of the barometric pressure sensors to detects the pressure difference. The cavity is sealed with PE-TEOS, which has a thin diaphragm (0.5 μm), which increase the sensitivity of the barometric sensors and reduces overall size of sensors. Heavily doped poly-Si used as the piezo-resistors of the barometric sensors, the FG and the micro-heater of the gas sensors at the same time.

To increase the sensitivity of the barometric pressure sensor, we proposed air pockets and a new design piezo-resistor. The barometric pressure sensor has a sensitivity of 2.47 μV/hPa, and has stably operated even over 100 repeated measurements. Also, the temperature and atmospheric pressure of the barometric pressure sensor are measured simultaneously, and the accurate air pressure is calculated using the MLP neural network.

The FET-type gas sensors fabricated with the barometric pressure sensor have a low-power localized micro-heater. In addition, under the micro-heater, the air-gap effectively prevented heat dissipation, thereby maintaining the proper temperature for gas detection. The micro-heater can heat up to 124 ºC with a power of 4 mW, and the detection of 0.5 ppm NO_2 gas is successfully achieved with the gas sensor.

Bibliography

[1] S. Santosh Kumar and B. D. Pant, “Polysilicon thin film piezoresistive pressure microsensor: design, fabrication and characterization”, *Microsystem Technologies*, vol.21, pp.1949-1958, 2015.

[2] Siro Sugiyama, T. Suzuki, Kazuo Kawahata, Kiyoshi Shimaoka, Mitsuharu Takigawa and Isemi Igarashi, “Micro-diaphragm pressure sensor”, *IEEE IEDM*, pp.184-187, 1986.

[3] Huiyang Yu, and Jianqiu Huang, “Design and Application of a High Sensitivity Piezoresistive Pressure Sensor for Low Pressure Conditions”. *Sensors*, vol.15, pp.22692-22704, 2015.

[4] Duy-Son Nguyen, Pit Pillatsch, Yiping Zhu, Igor Paprotny, Pual K. Wright, and Richard D. White, “MEMS-based Capacitive Pressure Sensors with Pre-stressed Sensing Diaphragms”, IEEE Sensors, pp.1-4, 2015.

[5] Bo Zhang and Pu-Xian Gao, “Metal Oxide Nanoarrays for Chemical Sensing: A Review of Fabrication Methods, Sensing Modes, and Their Inter-correlations”, *Frontiers in Materials*, vol.6, pp.1-20, 2019.

[6] M. C. Pereira, M. J. Martins, O. Bonnaud, “Thin Film Transistors Gas Sensors: Materials, Manufacturing Technologies and Test Results”, *Electronics and Electrical Engineering*, vol.89, pp.39-44, 2009.

[7] Kulwant Singh, Robin Joyce, Soney Varghese and J. Akhtar, "Fabrication of

electron beam physical vapor deposited polysilicon piezoresistive MEMS pressure sensor", *Sensors and Actuators A*, vol.223, pp.151-158, 2015.

[8] Tsung-Lin Chou, Chen-Hung Chu, Chun-Te Lin and Kuo-Ning Chiang, "Sensitivity analysis of packaging effect of silicon-based piezoresistive pressure sensor", *Sensors and Actuators A*, vol.152, pp.29-38, 2009.

[9] M. Olfatnia, T. Xu, J.M. Miao, L.S. Ong, X.M. Jing and L. Norford, "Piezoelectric circular microdiaphragm based pressure sensors", *Sensors and Actuators A*, vol.163, pp.32-36, 2010.

[10] T. Waber, W. Pahl, M. Schmidt, G. Feiertag, S. Stufler, R. Dudek, A. Leidl, “Temperature characterization of flip-chip packaged piezoresistive barometric pressure sensors”, *Microsystem Technologies*, vol.20, pp.861-867, 2014.

[11] Yozo Kanda and Akio Yasukawa, "Optimum design considerations for silicon piezoresistive pressure sensors", *Sensors and Actuators A*, vol.62, pp.539-542,1997.

[12] Dieter Maier-Schneider, J. Maibach and Emst Obermeier, "A new analytical solution for the load-deflection of square membranes", *Journal of Microelectromechanical System*, vol.4, pp.238-241, 1995.

[13] B.P. Gogoi and C.H. Mastrangelo, “A low-voltage force-balanced barometric pressure sensor”*, IEEE IEDM* , vol.96, pp.529-532, 1996.

[14] Masatoshi Esashi, Susumu Sugiyama, Kyoichi Ikeda, Yuelin Wang and Haruzo Mitashita, “Vacuum sealed silicon micromachined pressure sensors”, *Proceedings of the IEEE*, vol.86, pp.1627-1639, 1998.

[15] W.P Eaton and J.H Smith, “Micoromachined pressure sensors: review and recent developments”, *Smart Materials and Structures*, vol.6, pp.530-539, 1997.

[16] Orhan Akar, Tayfun Akin and Khalil Najafi, “A wireless batch sealed absolute capacitive pressure sensor”. *Sensors and Actuators A*, vol.95, pp.29-38, 2001.

[17] Shou-En Zhu, Murali Krishna Ghatkesar, Chao Zhang and G.C.A.M. Janssen, "Graphene based piezoresistive pressure sensor", *Applied Physics Letters*, vol.102, pp.161904, 2013.

[18] V.A. Gridchin, V.M. Lubimsky and M.P. Sarina, "Piezoresistive properties of polysilicon films", *Sensors and Actuators A*, vol.49, pp.67-72, 1995.

[19] D. Schubert and F.M. Schmidt, "Piezoresistive properties of polycrystalline and crystalline silicon films", *Sensors and Actuators*, vol.11, pp.145-155, 1987.

[20] Meng Nie, Qing-An Huang, Hui-Yang Yu, Ming Qin and Wei-Hua Li, “Complementary Metal-Oxide Semiconductor Compatible Capacitive Barometric Pressure Sensor”, *MEMS MOEMS*, vol.10, pp.013018, 2011.

[21] Ranjit Singh, Low Lee Ngo, Ho Soon Seng and Frederick Neo Chwee Mok “A Silicon Piezoresistive Pressure Sensor”, *Proceedings of the First IEEE International Workshop on Electronic Design, Test and Applications,* DELTA’02, 2002.

[22] Zhao-Hua Zhang, Yan-Hong Zhang, Li-Tian Liu, and Tian-Ling Ren, “A novel MEMS pressure sensor with MOSFET on chip”, *IEEE Sensors 2008 Conference*, pp.1564-1567, 2008.

[23] Dongkyu Jang, Yoonki Hong, Seongbin Hong, and Jong-Ho Lee, “A Novel Barometric Pressure Sensor Based on Piezoresistive Effect of Polycrystalline Silicon”, *Journal of Semiconductor Technology and Science*, vol.19, pp.172-177, 2019.

[24] Dongkyu Jang, Gyuweon Jung, Yujeong Jeong, Seongbin Hong, and Joing-Ho Lee, “Barometric Pressure Sensor with Air Pocket Integrated with MOSFETs on the Same Substrate”, *Journal of Semiconductor Technology and Science*, vol.20, pp.305-310, 2020.

[25] Dongkyu Jang, Gyuweon Jung, Yujeong Jeong, Seongbin Hong, Wonjun Shin, Ki Soo Chang, Chan Bae Jeong, Byung-Gook Park and Jong-Ho Lee, “Efficient Integration of Si FET-type Gas Sensors and Barometric Pressure Sensors on the Same Substrate, *IEEE IEDM*, pp.630-633, 2019.

[26] Yoonki Hong, Seongbin Hong, Dongkyu Jang, Yujeong Jeong, Meile Wu, Gyuweon Jung, Jong-Ho Bae, Jun Shik Kim, Ki Soo Chang, Chan Bae Jeong, Cheol Seong Hwang, Byung-Gook Park, and Jong-Ho Lee, “A Si FET-type Gas Sensor with Pulse-driven Localized Mico-heater for Low Power Consumption”, *IEEE IEDM*, pp.288-291, 2018.

[27] Angelo Marria Sabatini, and Vincenzo Genovese, “A Stochastic Approach to Noise Modeling for Barometric Altimeters”, *Sensors*, vol.13, pp.15692-15707, 2013.

[28] COMSOL Multiphysics®, v.5.3, www.comsol.com, Stockholm, Sweden.

[29] Chang-Hee Kim, In-Tak Cho, Jong-Min Shin, Kyu-Bong Choi, Jung-Kyu Lee, and Jong-Ho Lee, “A New Gas Sensor Based on MOSFET Having a Horizontal Floating-Gate”, *IEEE Electron Device Letters*, vol.35, pp.265-

267, 2014.

[30] D. Kahng, and S. M. SZE, “A Floating Gate and Its Application to Memory Devices”, *The Bell System Technical Journal*, pp.1288-1295, 1967.

[31] O. N. Tufte, P. W. Chapman, and D. Long, “Silicon Diffused –Element Piezoresistive Diaphragms”, *Journal of Applied Physics*, vol.33, pp.3322-3327, 1962.

[32] Liwei Lin, Huey-Chi, and Yen-Wen Lu, “A Simulation program for the sensitivity and linearity of piezoresistive pressure sensors”, *Journal of Microelectromechanical Systems*, vol.8, pp.514-522, 1999.

[33] E. Comimi, G. Faglia, G. Sberveglieri, Zhengwei Pan, and Zhong L. Wang, “Stable and highly sensitive gas sensors based on semiconducting oxide nanobelts”, *Applied Physics Letters*, vol.81, pp.1869-1871, 2002.

[34] E. Li, Zhixuan Cheng, Jiaqiang Xu, Qingyi Pan, Weijun Yu, and Yuliang Chu, “Indium Oxide with Novel Morphology: Synthesis and Application in C_2H_5OH Gas Sensing”, *Crystal Growth & Design*, vol.9, pp.2146-2151, 2009.

[35] Hyo-Joong Kim, Ji-Wook Yoon, Kwon-Il Choi, Ho Won Jang, Ahmad Umar, and Jong-Heun Lee, “Ultraselective and sensitive detection of xylene and toluene for monitoring indoor air pollution using Cr-doped NiO hierarchical nanostructures”, *Nanoscale*, vol.5, pp.7066-7073, 2013.

[36] Jungwoo Shin, Seon-Jin Choi, Inkun Lee, Doo-Young Youn, Chong Ook Park, Jong-Heun Lee, Harry L. Tuller, and Il-Doo Kim, “Thin-Wall Assembled SnO_2 Fibers Functionalized by Catalytic Pt Nanoparticles and

their Superior Exhaled-Breath-Sensing Properties for the Diagnosis of Diabetes". *Advanced Functional Materials*, vol.23, pp.2357-2367, 2013.

[37] M. Penza, R. Rossi, M. Alvisi, M. A. Signore, G. Cassano, D. Dimaio, R. Pentassuglia, E. Piscopiello, E. Serra, and M. Falconieri, "Characterization of metal-modified and vertically-aligned carbon nanotube films for functionally enhanced gas sensor applications", *Thin Solid Films*, vol.517, pp.6211-6216, 2009.

[38] Jing Li, Yijiang Lu, Qi Te, Martin Cinke, Jie Han, and M. Meyyappan, "Carbon nanotube sensors for gas and organic vapor detection", *Nano Letters*, vol.3, pp.929-933, 2003.

[39] Hyeun Joong Yoon, Do Han Jun, Jin Ho Yang, Zhixian Zhou, Sang Sik Yang, Mark Ming-Cheng Cheng, "Carbon dioxide gas sensor using a graphene sheet", *Sensors and Actuators B*, vol.157, pp.310-313, 2011.

[40] Ganhua Lu, Leonidas E Ocola, and Junhong Chen, "Reduced graphene oxide for room-temperature gas sensor", *Nanotechnology*, vol.20, p.445502, 2009.

[41] M. Donarelli, S. Prezioso, F. Perrozzi, F. Bisti, M. Nardone, L. Giancaterinim C. Cantalini, L. Ottaviano, "Response to NO_2 and other gases of resistive chemically exfoliated MoS_2-based gas sensors", *Sensors and Actuators B*, vol.207, pp.602-613, 2015.

[42] Kyung Yong Ko, Jeong-Gyu Song, Youngjun Kim, Taejin Choi, Sera Shin, Chang Wan Lee, Kyounghoon Lee, Jahyun Koo, Hoonkyung Lee, Jongbaeg Kim, Taeyoon Lee, Jusang Park, and Hyungjun Kim, "Improvement of Gas-Sensing Performance of Large-Area Tungsten Disulfide Nanosheets by Surface Functionalization", *American Chemical Society Nano*, vol.10,

pp.9287-9296, 2016.

[43] Li Xiao, Shengrui Xu, Geng Yu, and Shantang Liu, “Efficient hierarchical mixed Pd/SnO_2 porous architecture deposited microheater for low power ethanol gas sensor”, *Sensors and Actuators B*, vol.255, pp.2002-2010, 2010.

[44] Hu Long, Anna Harley-Trochimczyk, Tianyi Hem Thang Pham, Zirong Tang, Tielin Shi, Alex Zettl, William Mickelson, Carlo Carraro, and Roya Maboudian, “In Situ Localized Growth of Porous Tin Oxide Films on Low Power Micoheater Platform for Low Temperature CO Detection”, *American Chemical Society Sensors*, vol.1, pp.339-343. 2016.

[45] Thorsten Wagner, Stefanie Haffer, Christian Weinberger, Dominik Klaus, and Michael Tiemann, “Mesoporous materials as gas sensors”, *Chemical Society Reviews*, vol.42, pp.4036-4053, 2013.

[46] Jane Hodgkinson and Ralph P. Tatam, “Optical gas sensing: a review”, *Measurement Science and Technology*, vol.24, p.012004, 2013.

[47] R. Rubio, J. Santander, L. Fonseca, N. Sabate, I. Gracia, C. Cane, S. Udina, and S. Marco, “Non-selective NDIR array for gas detection”, *Sensors and Actuators B*, vol.127, pp.69-73, 2007.

[48] Ayunshi Paliwal, Anjali Sharma, Monika Tomar, and Vinay Gupta, “Room temperature detection of NO_2 gas using optical sensor based on surface plasmon resonance technique”, *Sensors and Actuators B*, vol.218, pp.497-503, 2015.

[49] Liuzheng Ma, Ling Wang, Ruipeng Chen, Keke Chang, Shun Wang, Xinran Hu, Xiaohui Sun, Zhaohui Lu, Haifeng Sun, Qingqian Guo, Min Jiang, and

Jiandong Hu, “A Low Cost Compact Measurement System Constructed Using a Smart Electrochemical Sensor for the Real-Time Discrimination of Fruit Ripening”, Sensors, vol.16, pp.501-512, 2016.

[50] Michael J. Tierney and Hyun-Ok L. Kim, “Electrochemical Gas Sensor with Extremely Fast Response Times”, *Analytical Chemistry*, vol.65, pp.3435-3440, 1993.

[51] Hithesh K. Gatty, Simon Leijonmarck, Mikael Antelius, Goran Stemme, and Niclas Roxhed, “An amperometric nitric oxide sensor with fast response and ppb-level concentration detection relevant to asthma monitoring”, *Sensors and Actuators B*, vol.209, pp.639-644, 2015.

[52] Frank Liao, Christopher Chen, and Vivek Subramanian, “Organic TFTs as gas sensors for electronic nose applications”, *Sensors and Actuators B*, vol.107, pp.849-855, 2005.

[53] Hsiao-Wen Zan, Chang-Hung Li, Chun-Cheng Yeh, Ming-Zhi Dai, Hsin-Fei Meng, and Chuang-Chuang Tsai, “Room-temperature-operated sensitive hybrid gas sensor based on amorphous indium gallium zinc oxide thin-film transistors”, *Applied Physics Letters*, vol.98, p.253503, 2011.

[54] Qiyuan He, Zhiyuan Zeng, Zongyou Yin, Hai Li, Shixin Wu, Xiao Huang, and Hua Zhang, “Fabrication of flexible MoS_2 thin-film transistor arrays for practical gas-sensing applications”, *Small*, vol.8, pp.2994-2999, 2012.

[55] I. Lundstrom, S Shivaraman, C. Svensson, and L. Lundkvist, “A hydrogen-sensitive MOS field-effect transistor”, *Applied Physics Letters*, vol.26, pp.55-57, 1975.hhhh

[56] M. S. Shivaraman, “Detection of H_2S with Pd-gate MOS field-effect transistors”, *Journal of Applied Physics*, vol.47, pp.3592-3593, 1976.

[57] Ulf Ackelid, M. Armgarth, A. Spetz, and I. Lundstrom, “Ethanol Sensitivity of Palladium-Gate Metal-Oxide-Semiconductor Structures”, *IEEE Electron Device Letters*, vol.7, pp.353-355, 1981.

[58] M. Josowicz, and J. Jannata, “Suspended Gate Field Effect Transistors Modified with Polyptrrole as Alcohol Sensor”, *Analytical Chemistry*, vol.58, pp.514-517, 1986.++

[59] Sentaurus™, www.synopsys.com, Synopsys Inc, USA.

요약(국문초록)

사물 인터넷 (IoT) 시대를 맞이하여 삶의 질을 개선하기 위한 센서 기술들이 점차 중요해지고 있다. 특히, 각종 스마트 기기들을 비롯한 자동차 및 가전 제품에 대한 센서 기술들이 필수적이 되고 있다. 아울러, 다양한 종류의 센서들의 통합 및 집적 기술이 주목받고 있다. 여러 유형의 센서들을 단일 기판에서 CMOS 회로와 효율적으로 통합하면 전력 소모를 줄일 수 있으며, 제조 단가 또한 낮출 수 있다. 다양한 센서기술 중 가스 센서는 유해 가스 감지뿐만 아니라 실내 공기 질 개선 및 질병 감지에 사용될 것으로 예상된다. 종래의 저항 형 가스 센서는 구조가 간단하며 제조 공정이 단순하지만 크기가 크고 전력 소비가 높은 편이다. 한편, FET 형 가스 센서는 매우 작은 크기로 제작이 가능하며 CMOS 회로와 호환 가능하다. 또한 내장된 마이크로 히터 (Micro-Heater)를 사용하게 되면 FET 형 가스 센서의 전력 소비를 최소화 시킬 수 있다.

본 논문에서는 기압 센서와 Si FET 형 가스 센서를 MOSFET 제조 공정기술을 사용하여 단일 실리콘 (Silicon) 기판에 효율적으로 집적하였다. 제작된 기압 센서는 온도 센서를 내장하고 있어서 주변 온도에 따른 대기압을 정확하게 측정 가능하다. 또한 FET 형 가스 센서는 4 mW의 전력으로 최대

124 ˚C까지 가열 할 수 있는 국부화 된 마이크로 히터를 내장하고 있다. 이 가스 센서로 이산화 질소가스 (NO_2)의 농도를 측정하였다.

2.5 μm 깊이의 에어 갭 (Air-gap)을 Si 기판에 형성하고 이 에어 갭은 기압 센서의 공동 (Cavity) 및 FET 형 가스 센서의 절연 층으로 사용하였다. 또한, 붕소(Boron) 이온을 주입한 다결정 실리콘 (Poly-Si)은 기압 센서 및 온도 센서의 전극, FET 형 가스 센서의 플로팅 게이트 (Floating-gate), 그리고 마이크로 히터의 전극으로 동시에 사용하였다. 이러한 방식으로 기압 센서, FET 형 가스센서는 CMOS 호환 제조 공정을 사용하여 효율적으로 단일기판에 집적하였다. 기압 센서는 주변 온도와 대기압을 동시에 측정 할 수 있는 온도 센서를 내장하고 있으며, 주변 온도에 따른 대기압을 신경망을 통하여 97.5 %의 정확도로 측정할 수 있다.

주요어: 센서 집적, 가스 센서, 기압 센서, 에어 갭.

학번: 2016-30211